ATLAS CONF Note

ATLAS-CONF-2018-040

July 24, 2018

Search for bottom-squark pair production with the ATLAS detector in final states containing Higgs bosons, b-jets and missing transverse momentum in pp collisions at $\sqrt{s} = 13$ TeV

The ATLAS Collaboration

The result of a search for the production of the supersymmetric partner of the bottom-quark ($\tilde{b}_1$) using 79.8 fb^{-1} of data collected at $\sqrt{s} = 13$ TeV by the ATLAS detector in Run 2 is reported. In the supersymmetric scenarios considered the bottom-squarks decay to a b-quark and the second lightest neutralino, $\tilde{b}_1 \rightarrow b + \tilde{\chi}_2^0$. The $\tilde{\chi}_2^0$ is assumed to subsequently decay with 100% branching ratio to the Standard-Model-like Higgs boson (h) and the lightest neutralino: $\tilde{\chi}_2^0 \rightarrow h + \tilde{\chi}_1^0$. The $\tilde{\chi}_1^0$ is assumed to be the lightest supersymmetric particle (LSP) and is stable. Two signal mass configurations are targeted: the first has a constant LSP mass of 60 GeV; and the second has a constant mass difference between the $\tilde{\chi}_2^0$ and $\tilde{\chi}_1^0$ of 130 GeV. The final states considered contain zero leptons, three or more b-jets, and large missing transverse momentum. No significant excess of events over the Standard Model background expectation is observed in any of the signal regions considered. Limits at the 95% confidence level are placed in the simplified models considered, and bottom-squarks with mass up to 1400 GeV are excluded.

ATLAS-CONF-2018-040
25 July 2018

1 Introduction

Supersymmetry (SUSY) [1, 2, 3, 4, 5, 6] provides an extension of the Standard Model (SM) that solves the hierarchy problem [7, 8, 9, 10] by introducing partners of the known bosons and fermions. In R-parity-conserving models [11], SUSY particles are produced in pairs and the lightest supersymmetric particle (LSP) is stable and provides a candidate for dark matter [12, 13]. For a large selection of models, the LSP is the lightest neutralino ($\tilde{\chi}_1^0$). Naturalness considerations suggest that the supersymmetric partners of the third-generation quarks are light [14, 15]. Such considerations lead to the lightest bottom squark ($\tilde{b}_1$) and lightest top squark ($\tilde{t}_1$) mass eigenstates[1] being significantly lighter than the other squarks and the gluinos. As a consequence, $\tilde{b}_1$ and $\tilde{t}_1$ could be pair-produced with relatively large cross-sections at the Large Hadron Collider (LHC). Depending on the mass hierarchy considered it is possible that the $\tilde{b}_1$ and $\tilde{t}_1$ could decay with higgs bosons in the final state, allowing the higgs boson to be used as a probe for new physics.

This paper presents a search for pair production of bottom squarks decaying to the LSP via a complex decay chain containing the second lightest neutralino ($\tilde{\chi}_2^0$), and the SM-like Higgs boson (h): $\tilde{b}_1 \rightarrow b + \tilde{\chi}_2^0$ and subsequently $\tilde{\chi}_2^0 \rightarrow h + \tilde{\chi}_1^0$. Such a decay hierarchy is predicted in minimal supersymmetric extension of the SM (MSSM) [16, 17] models, when the LSP is considered to be bino-like and the $\tilde{\chi}_2^0$ is a wino-higgsino mixture, which enhances the BR($\tilde{\chi}_2^0 \rightarrow h + \tilde{\chi}_1^0$). The Higgs boson mass is taken to be 125 GeV. The decay into a pair of b-quarks is assumed to be SM-like (BR = 58% [18]), although it could be enhanced or reduced in the MSSM. This search is performed using simplified model scenarios [19, 20] and Figure 1 illustrates the targeted model. The final states are characterised by a unique signature which contains many jets, up to six that can be identified as originating from the fragmentation of b-quarks (referred to as b-jets), and missing transverse momentum ($\mathbf{p}_{\mathrm{T}}^{\mathrm{miss}}$, the magnitude thereof referred to as $E_{\mathrm{T}}^{\mathrm{miss}}$).

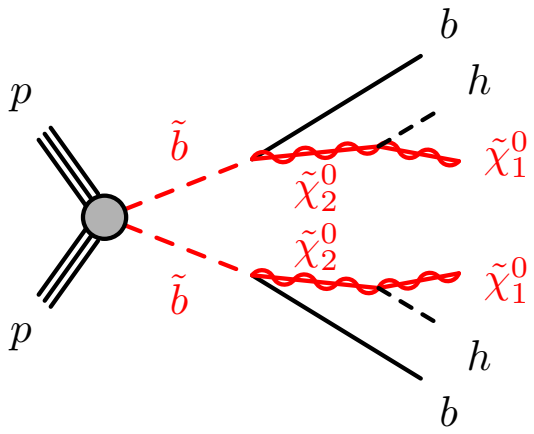

Figure 1: Graphical representation of the SUSY signal targeted by this analysis. Bottom squarks are produced in pairs and subsequently decay to $b\tilde{\chi}_2^0$ with 100% BR. The two $\tilde{\chi}_2^0$ particles decay to $h\tilde{\chi}_1^0$ also with 100% BR.

In the first set of simplified models, already considered in Run 1 by the ATLAS collaboration [21], the mass of the $\tilde{\chi}_1^0$ is fixed at 60 GeV. The bottom squark and $\tilde{\chi}_2^0$ masses vary in the ranges 150-1500 GeV and 200-1100 GeV, respectively. The assumption on the $\tilde{\chi}_1^0$ mass is motivated by Dark Matter relic density measurements and is favoured in Higgs-pole annihilation scenarios where $m_{\tilde{\chi}_1^0} \simeq m_h/2$. The previous

[1] The scalar partners of the left-handed and right-handed chiral components of the bottom quark ($\tilde{b}_{\mathrm{L,R}}$) or top quark ($\tilde{t}_{\mathrm{L,R}}$) mix to form mass eigenstates for which $\tilde{b}_1$ and $\tilde{t}_1$ are defined as the lighter of the two states.

search performed by ATLAS using the Run 1 LHC dataset excluded bottom squark masses up to 750 GeV in this scenario.

The second set of SUSY models assume a fixed mass difference between the $\tilde{\chi}_2^0$ and $\tilde{\chi}_1^0$, sufficient to produce an on-shell Higgs boson. The $\Delta m(\tilde{\chi}_2^0, \tilde{\chi}_1^0)$ is set to 130 GeV, whilst bottom squark and $\tilde{\chi}_1^0$ masses vary in the ranges 400 to 1500 GeV and 1 to 800 GeV, respectively. A similar scenario has been considered by the CMS collaboration in Ref. [22], where the $h \to \gamma\gamma$ decay mode was exploited. Bottom squark masses up to 450 GeV have been excluded. No prior ATLAS searches have been performed targeting these models.

2 ATLAS detector

The ATLAS detector [23] is a multi-purpose particle physics detector with a forward-backward symmetric cylindrical geometry and nearly 4π coverage in solid angle.[2] The inner tracking detector consists of pixel and silicon microstrip detectors covering the pseudorapidity region $|\eta| < 2.5$, surrounded by a transition radiation tracker which enhances electron identification in the region $|\eta| < 2.0$. Between Run 1 and Run 2, a new inner pixel layer, the insertable B-layer [24], was added at a mean sensor radius of 3.3 cm. The inner detector is surrounded by a thin superconducting solenoid providing an axial 2 T magnetic field and by a fine-granularity lead/liquid-argon (LAr) electromagnetic calorimeter covering $|\eta| < 3.2$. A steel/scintillator-tile calorimeter provides hadronic coverage in the central pseudorapidity range ($|\eta| < 1.7$). The endcap and forward regions ($1.5 < |\eta| < 4.9$) of the hadronic calorimeter are made of LAr active layers with either copper or tungsten as the absorber material. An extensive muon spectrometer with an air-core toroidal magnet system surrounds the calorimeters. Three layers of high-precision tracking chambers provide coverage in the range $|\eta| < 2.7$, while dedicated fast chambers allow triggering in the region $|\eta| < 2.4$. The ATLAS trigger system consists of a hardware-based level-1 trigger followed by a software-based high-level trigger [25].

3 Data and simulated event samples

The dataset used corresponds to a total of 79.8 fb^{-1} of proton-proton (pp) collision data collected by the ATLAS detector with a centre-of-mass energy of 13 TeV and a 25 ns proton bunch crossing interval in the period between 2015 and 2017. All detector subsystems were required to be operational during data recording. For this dataset the average number of interactions per bunch crossing $\langle\mu\rangle = 31.9$. The uncertainty in the combined 2015-2017 integrated luminosity is 2.0%. It is derived, following a methodology similar to that detailed in Ref. [26], from calibrations of the luminosity scale using x-y beam-separation scans performed in August 2015, May 2016 and July 2017 (the results for 2017 are still preliminary).

[2] ATLAS uses a right-handed coordinate system with its origin at the nominal interaction point in the centre of the detector. The positive x-axis is defined by the direction from the interaction point to the centre of the LHC ring, with the positive y-axis pointing upwards, while the beam direction defines the z-axis. Cylindrical coordinates (r, ϕ) are used in the transverse plane, ϕ being the azimuthal angle around the z-axis. The component of momentum in the transverse plane is denoted by p_{T}. The pseudorapidity η is defined in terms of the polar angle θ by $\eta = -\ln\tan(\theta/2)$. Rapidity is defined as $y = 0.5\ln[(E + p_z)/(E - p_z)]$ where E denotes the energy, and p_z is the component of the momentum along the beam direction. The separation in η, ϕ space of two objects is given by $\Delta R = \sqrt{(\Delta\phi)^2 + (\Delta\phi)^2}$.

Events used in this analysis are required to pass a $E_{\mathrm{T}}^{\mathrm{miss}}$ trigger [27]. This trigger is fully efficient for events with reconstructed $E_{\mathrm{T}}^{\mathrm{miss}} > 250$ GeV. Additional single-lepton triggers requiring electrons or muons are used for selections employed to aid in the estimate of the SM backgrounds, with a selection of $p_{\mathrm{T}}(\ell) > 27$ GeV used to ensure the trigger is fully efficient.

Dedicated Monte-Carlo (MC) samples of simulated events are used to model SM processes and estimate the expected signal yields. All samples are produced using the ATLAS simulation infrastructure [28] and GEANT4 [29], or a faster simulation based on a parameterization of the calorimeter response and GEANT4 for the other detector systems [30]. The simulated events are reconstructed with the same algorithms as that used for data, and contain a realistic modelling of pileup interactions.

SUSY signal samples are generated with MadGraph v2.3.3 [31] at leading order (LO) and interfaced to PYTHIA v8.230 [32] with the A14 [33] set of tuned parameters (tune) for the modeling of the parton showering (PS), hadronization and underlying event. The matrix element (ME) calculation is performed at tree level and includes the emission of up to two additional partons. The ME–PS matching is done using the CKKW-L [34] prescription, with a matching scale set to one quarter of the bottom squark mass. The NNPDF23LO [35] parton distribution function (PDF) set is used. The cross-sections used to evaluate the signal yields are calculated to next-to-leading order (NLO) accuracy in the strong coupling constant, adding the resummation of soft gluon emission at next-to-leading-logarithmic accuracy (NLO+NLL) [36, 37, 38]. The nominal cross-section and uncertainty are taken as the midpoint and half-width of an envelope of cross-section predictions using different PDF sets and factorization and renormalization scales, as described in Ref. [39].

The SM backgrounds considered in this analysis are: $t\bar{t}$ pair production; single-top production; Z+jets; W+jets; $t\bar{t}$ production with an electroweak (ttV), or Higgs (ttH), boson; and diboson production. The samples are simulated using different MC generator programs depending on the process. Pair production of top quarks, $t\bar{t}$, is generated using POWHEG v2 [40] interfaced with PYTHIA8 and the A14 tune with the NNPDF23LO PDF set for the ME calculations. The h_{damp} parameter in POWHEG, which controls the p_{T} of the first additional emission beyond the Born level and thus regulates the p_{T} of the recoil emission against the $t\bar{t}$ system, is set to 1.5 times the top-quark mass ($m_t = 172.5$ GeV) as a result of studies documented in Ref. [41]. The generation of single top quarks in the Wt, s-channel and t-channel is performed by POWHEG v2 similarly to $t\bar{t}$ samples. For all processes involving top quarks, top quark spin correlations are preserved. All events with at least one leptonically decaying W boson are retained. Fully hadronic $t\bar{t}$ and single-top events do not contain sufficient $E_{\mathrm{T}}^{\mathrm{miss}}$ to contribute significantly to the background. The production of $t\bar{t}$ pairs in association with electroweak vector bosons (W, Z) or Higgs bosons is modeled by samples generated at NLO using MadGraph v2.2.3 and showered with PYTHIA v8.212. Events containing W or Z bosons with associated jets, including jets from the fragmentation of b- and c-quarks, are simulated using the SHERPA v2.2.1 [42] generator. Matrix elements are calculated for up to two additional partons at NLO and four partons at LO using the Comix [43] and OpenLoops [44] matrix element generators and merged with the SHERPA PS [45] using the ME+PS@NLO prescription [46]. The NNPDF30NNLO [35] PDF set is used in conjunction with a dedicated PS tune developed by the SHERPA authors. Diboson processes are also simulated using the SHERPA generator using the NNPDF30NNLO PDF set in conjunction with a dedicated PS tune developed by the SHERPA authors. They are calculated for up to one (ZZ) or zero (WW, WZ) additional partons at NLO and up to three additional partons at LO. Other potential sources of backgrounds, such as the production of three or four top quarks or three gauge bosons, are found to be negligible. Finally, contributions from multijet background are estimated from data using a jet smearing procedure described in Ref. [47] and are found to be negligible in all regions.

All background processes are normalized to the best available theoretical calculation for their respective cross-sections. The NLO $t\bar{t}$ inclusive production cross section is corrected to the theory prediction at next-to-next-to-leading order (NNLO) in QCD including the resummation of next-to-next-to-leading logarithmic (NNLL) soft-gluon terms calculated using Top++2.0 [48, 49, 50, 51, 52, 53, 54]. Samples of single-top-quark events are normalized to the NLO cross-sections reported in Refs. [55, 56, 57] for the s-, t- and Wt-channels, respectively.

For all samples, except those generated using SHERPA [42], the EvtGen v1.2.0 [58] program is used to simulate the properties of the bottom- and charm-hadron decays. Several samples, mostly top production, produced without detector simulation are employed to estimate systematic uncertainties associated with the specific configuration of the MC generators used for the nominal SM background samples. They include variations of the renormalization and factorization scales, the CKKW-L matching scale, as well as different PDF sets and fragmentation/hadronization models.

4 Event Reconstruction

This search is based upon a selection of events with many b-jets, large missing transverse momentum and requiring no charged leptons (electrons and muons) in the final state. All events are required to have a reconstructed primary vertex which is consistent with the beamspot envelope and consists of at least two associated tracks in the inner detector with p_{T} >0.4 GeV. If more than one vertex passing the above requirements is found, the one with the largest sum of the squares of transverse momenta of associated tracks [59] is chosen.

Jet candidates are reconstructed from three-dimensional clusters of energy in the calorimeter [60] with the anti-k_t jet algorithm [61, 62] using a radius parameter of 0.4. The application of a jet energy scale (JES) derived from data and simulation [63] is used to calibrate the reconstructed jets. A set of quality criteria are applied to identify jets which arise from non-collision sources or detector noise [64], and any event which contains a jet failing this criteria is removed. Additional jets which arise from pile-up interactions are rejected by applying additional track-based selections to jets with $p_{\mathrm{T}} < 60$ GeV and $|\eta| < 2.4$, and the jet momentum is corrected by subtracting the expected average energy contribution from pile-up using the jet area method [65]. Jets are classified as either "baseline" or "signal", with baseline jets required to have $p_{\mathrm{T}} > 20$ GeV and $|\eta| < 4.8$. Signal jets are selected after resolving overlaps, as described later in this section, with electrons and muons and must pass tighter requirements of $p_{\mathrm{T}} > 30$ GeV and $|\eta| < 2.8$.

Signal jets are identified as b-jets if they are tagged by a multivariate algorithm which uses a selection of inputs including information about the impact parameters of inner detector tracks, the presence of displaced secondary vertices and the reconstructed flight paths of b- and c-hadrons inside the jet [66]. The b-tagging working point with 77% efficiency, as determined in a sample of simulated $t\bar{t}$ events, was chosen as part of the optimisation procedure, the corresponding mis-identification rate is 25% for c-jets and 0.88% for light-jets. To compensate for differences between data and MC simulation in the b-tagging efficiencies and mis-tag rates, correction factors are derived from data and applied to the samples of simulated events [66]. Candidate b-jets are required to be signal jets with a tighter selection on pseudorapidity of $|\eta| < 2.5$.

Electron candidates are reconstructed from energy clusters in the electromagnetic calorimeter matched to a track in the inner detector and are required to satisfy a set of "loose" quality criteria [67, 68, 69]. They are also required to lie within the fiducial volume $|\eta| < 2.47$ and have $p_{\mathrm{T}} > 7$ GeV. Muon candidates are reconstructed by matching tracks in the inner detector with tracks in the muon spectrometer. Muon

candidates which have a transverse (longitudinal) impact parameter with respect to the primary vertex larger than 0.2 mm (1 mm) are rejected to suppress muons from cosmic rays. Muon candidates are also required to satisfy "medium" quality criteria [70] and have $|\eta| < 2.5$ and $p_{\mathrm{T}} > 6$ GeV. Electron (muon) candidates are matched to the primary vertex by requiring the transverse impact parameter (d_0) to satisfy $|d_0|/\sigma(d_0) < 5$ (3), and the longitudinal impact parameter (z_0) to satisfy $|z_0 \sin\theta| < 0.5$ mm for both the electrons and muons. Lepton candidates remaining after resolving overlaps with baseline jets are called "baseline" leptons. In the control regions where lepton identification is required, "signal" leptons are chosen from the baseline set with $p_{\mathrm{T}} > 27$ GeV to ensure full efficiency of the single-lepton triggers and are required to be isolated from other activity in the detector using a criterion designed to accept at least 95% of leptons from Z boson decays as detailed in Ref. [71]. Signal electrons are further required to satisfy "tight" quality criteria. The MC events are corrected to account for differences in the lepton trigger, reconstruction and identification efficiencies between data and MC simulation.

Possible overlaps between baseline electrons, muons and jets are resolved by firstly removing electron candidates which share an inner detector track with a muon candidate. Jet candidates are then removed if they are within $\Delta R = \sqrt{(\Delta y)^2 + (\Delta\phi)^2} < 0.2$ of an electron candidate; next electron candidates are discarded if they are within $\Delta R = 0.4$ of a jet. Muons are discarded if they lie within $\Delta R = 0.4$ of any remaining jet, except for the case where the number of tracks associated with the jet is less than three, where the muon is kept and the jet is discarded.

Fully-reconstructed tau leptons decaying hadronically are not considered but the following tau veto procedure is applied to reject events which contain tau-like objects. Tau candidates (τ_{cand}) are defined as jet candidates which have $|\eta| < 2.5$ and ≤ 4 inner detector tracks of $p_{\mathrm{T}} > 500$ MeV. If an event contains a tau candidate with a small azimuthal distance to the $\mathbf{p}_{\mathrm{T}}^{\mathrm{miss}}$ ($\Delta\phi(E_{\mathrm{T}}^{\mathrm{miss}}, \tau_{\mathrm{cand}}) < \pi/5$), then the event is vetoed.

The missing transverse momentum $\mathbf{p}_{\mathrm{T}}^{\mathrm{miss}}$ (with its modulus $E_{\mathrm{T}}^{\mathrm{miss}}$) is defined as the negative vector sum of the p_{T} of all selected and calibrated physics objects (electrons, muons, photons [72] and jets) in the event, with an extra term added to account for soft energy in the event which is not associated with any of the selected objects [73]. This soft term is calculated from inner detector tracks with p_{T} above 400 MeV matched to the primary vertex to make it more robust against pile-up contamination [74, 75].

5 Analysis strategy

Three sets of non-orthogonal signal regions (SRs) are defined and optimized to target different mass hierarchies of the SUSY particles involved. They exploit various discriminating observables and algorithms developed to explicitly reconstruct Higgs boson candidates in the decay chain. Events with charged leptons are vetoed in all SRs, whilst events with either one, or two, charged leptons are used to define control and validation regions (CRs and VRs) employed to aid in the estimate of the main SM backgrounds, which are found to be $t\bar{t}$ and Z boson production in association with b-jets, depending upon the region under consideration. The method of estimating these backgrounds is described in Section 6.

The optimization procedure, aiming to maximize the efficiency to retain bottom-squark pair production events and reduce SM background contributions, is performed considering the two simplified model scenarios introduced in Section 1. As the $h \rightarrow bb$ decay mode is considered, the final state contains a large jet multiplicity, with many of these jets originating from b-quarks and large $E_{\mathrm{T}}^{\mathrm{miss}}$ from the neutralinos.

The event selection criteria are defined on the basis of kinematic requirements for the objects described in the previous section and event variables described below. Signal jets are used and are ordered according to decreasing p_{T}.

- N_{jets}: the number of signal jets.
- $N_{\mathrm{b-jets}}$: the number of b-tagged jets.
- $\min \Delta\phi(\mathrm{jet}_{1-4}, \mathbf{p}_{\mathrm{T}}^{\mathrm{miss}})$: the minimum azimuthal distance between the four highest p_{T} jets and the $\mathbf{p}_{\mathrm{T}}^{\mathrm{miss}}$ proves to be a powerful discriminating tool against multijet background events containing a large amount of $E_{\mathrm{T}}^{\mathrm{miss}}$ due to mismeasured jets. Typically, multijet background events exhibit low values of this variable and studies using data-driven multijet estimates indicate that a selection of $\min \Delta\phi(\mathrm{jet}_{1-4}, \mathbf{p}_{\mathrm{T}}^{\mathrm{miss}}) > 0.4$ is sufficient to reduce the multijet background to a negligible level.
- $\Delta\phi(j_1, \mathbf{p}_{\mathrm{T}}^{\mathrm{miss}})$: the azimuthal distance between the highest p_{T} jet and the $\mathbf{p}_{\mathrm{T}}^{\mathrm{miss}}$. This variable is used to select events where the $\mathbf{p}_{\mathrm{T}}^{\mathrm{miss}}$ is expected to be recoiling against the leading jet.
- m_{eff} [GeV]: the effective mass of an event is defined as the scalar sum of the p_{T} of all signal jets and the $E_{\mathrm{T}}^{\mathrm{miss}}$, i.e.:

$$m_{\mathrm{eff}} = \sum_{i \leq N_{\mathrm{jets}}} (p_{\mathrm{T}}^{\mathrm{jet}})_i + E_{\mathrm{T}}^{\mathrm{miss}}. \tag{1}$$

- $\mathcal{S}$: referred to as the object-based $E_{\mathrm{T}}^{\mathrm{miss}}$ Significance [76] and defined as follows: $\mathbf{p}_{\mathrm{T}}^{\mathrm{miss}}$ is the vector of missing momentum in the transverse plane and σ_{L} is the total expected longitudinal (parallel to the $\mathbf{p}_{\mathrm{T}}^{\mathrm{miss}}$) momentum resolution of all jets and leptons at a given p_{T} and $|\eta|$ which is parameterised using Monte Carlo simulation which well reproduces the resolution measured in data. The total expected momentum resolution is calculated as the sum of the jets and leptons in the event, which is subsequently projected onto a basis parallel and transverse to the $\mathbf{p}_{\mathrm{T}}^{\mathrm{miss}}$. The quantity ρ_{LT} is a correlation factor between each jet's or lepton's longitudinal and transverse momentum resolution (again with respect to the $\mathbf{p}_{\mathrm{T}}^{\mathrm{miss}}$). The $\mathcal{S}$ is used to discriminate events where the $E_{\mathrm{T}}^{\mathrm{miss}}$ arises from poorly measured particles (and jets) from events where the $E_{\mathrm{T}}^{\mathrm{miss}}$ arises from invisible particles in the final state.

$$\mathcal{S} = \sqrt{\frac{|\mathbf{p}_{\mathrm{T}}^{\mathrm{miss}}|^2}{\sigma_{\mathrm{L}}^2(1-\rho_{\mathrm{LT}}^2)}}. \tag{2}$$

Additional selections on the p_{T} of the leading jet and of the leading b-tagged jet are also applied as detailed in the following sub-sections. In all regions, events containing baseline leptons with $p_{\mathrm{T}} > 10$ GeV are vetoed, as well as events containing τ candidates as described in Section 4. Only events with $E_{\mathrm{T}}^{\mathrm{miss}} > 250$ GeV are retained to ensure full efficiency of the trigger.

The event kinematics targeted by the three SRs are depicted in Figure 2. The SRA region targets the "bulk" region of both signal mass scenarios, with moderate to high mass splitting between the $\tilde{b}_1$ and $\tilde{\chi}_2^0$. In these scenarios all of the b-jets, from both the bottom-squark and Higgs decays, are at a relatively high p_{T} and can be resolved in the detector. In these scenarios the b-jets from the Higgs boson can be isolated by removing the high p_{T} b-jets from the bottom-squark decays and checking the angular separation between the remaining b-jets. The SRB region targets the phase space of the $\Delta m(\tilde{\chi}_2^0, \tilde{\chi}_1^0) = 130$ GeV scenario, where there is a small mass splitting between the $\tilde{b}_1$ and $\tilde{\chi}_2^0$, referred to as the "compressed" region. An initial state radiation (ISR)-like selection is used where the small mass splitting between the bottom-squark

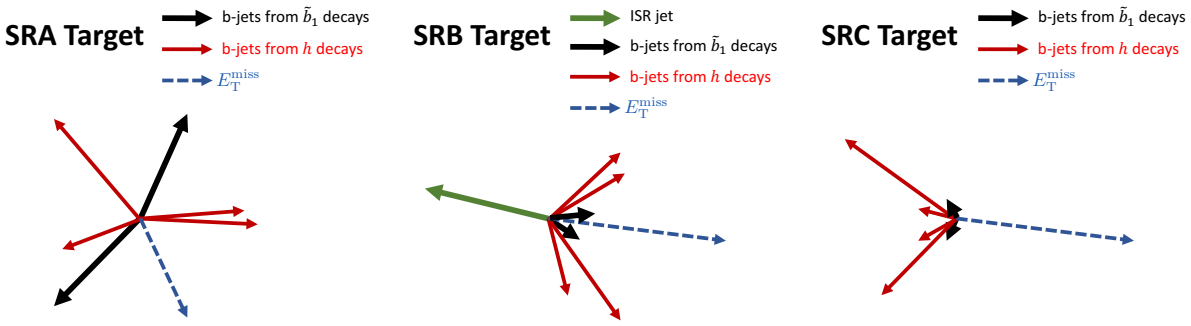

(a) SRA (b) SRB (c) SRC

Figure 2: The different event kinematics targeted by the three SRs: (a) kinematics in the bulk region, with high p_{T} b-jets arising from the bottom-squark decay; (b) kinematics in the compressed region of the $\Delta m(\tilde{\chi}_2^0, \tilde{\chi}_1^0) = 130\,\mathrm{GeV}$ scenario with soft b-jets from the bottom-squark; (c) kinematics in the compressed region of the $\Delta m(\tilde{\chi}_1^0) = 60\,\mathrm{GeV}$ scenario with soft b-jets from the Higgs decays.

and neutralino leads to very soft b-jets from the bottom-squark decay, which are difficult to reconstruct. In this scenario it is possible to reconstruct both Higgs bosons using angular separation methods. Finally the SRC region targets the "compressed" region of the $m(\tilde{\chi}_1^0) = 60\,\mathrm{GeV}$ signal scenario, where the mass splitting between the $\tilde{b}_1$ and $\tilde{\chi}_2^0$ is small. The b-jets from the bottom-squark decay are relatively soft and as such a lower b-jet multiplicity is used in this region, when compared to the A- and B-type selections. Additionally the visible system (b-jets from the bottom-squark decay and Higgs decay) is produced back to back with the reconstructed $\mathbf{p}_{\mathrm{T}}^{\mathrm{miss}}$.

5.1 SRA selections

To exploit the kinematic properties of the signal over the large range of $\tilde{b}_1$, $\tilde{\chi}_2^0$ and $\tilde{\chi}_1^0$ masses explored, incremental thresholds are imposed on the main discriminating variable, m_{eff}, resulting in three mutually exclusive regions ($1<m_{\mathrm{eff}}<1.2$, $1.2<m_{\mathrm{eff}}<1.5$ and $m_{\mathrm{eff}}>1.5$ TeV) labelled as SRA-L, -M and -H respectively. The selection criteria for the SRAs are summarised in Table 1. At least four b-tagged jets are required. To discriminate against multijet background, events where the $\mathbf{p}_{\mathrm{T}}^{\mathrm{miss}}$ is aligned with a jet in the transverse plane are rejected by requiring $\min \Delta\phi(\mathrm{jet}_{1-4}, \mathbf{p}_{\mathrm{T}}^{\mathrm{miss}}) > 0.4$. At least one of the two Higgs boson candidates in the event is identified using a single-Higgs boson reconstruction algorithm referred to as *MaxMin*. The expected signal topology is exploited using a two-step procedure to first attempt to remove the high-p_{T} b-jets from the bottom-squark decay, then using the remaining b-jets to reconstruct a Higgs boson in the decay chain. This procedure is implemented as follows: first, pairs of b-jets are formed by iterating through all of the b-jets in the event, and the one with the largest separation in η-ϕ (ΔR) is designated as arising from the bottom-squark decay; second, among the remaining pairs, the one with lowest ΔR is identified as a possible Higgs boson candidate and its invariant mass calculated. The following ΔR and mass quantities are defined:

- $\Delta R_{\mathrm{max}}(b, b)$: the distance in η-ϕ between the two b-jets with the maximal angular separation which are most likely to originate from the initial decay of the $\tilde{b}_1$;

- $\Delta R_{\text{max}-\text{min}}(b, b)$: the distance in η-ϕ between the two b-jets with the minimum angular separation which are most likely to originate from the same Higgs decay, selected out of the remaining b-jets;
- $m(h_{\text{cand}})$: the invariant mass of the two b-jets closest in angular separation, used to reconstruct the Higgs boson mass. A one-sided selection $m(h_{\text{cand}})$ is used, as for the majority of signals the distribution peaks around the Higgs mass, but in scenarios where the incorrect combination of b-jets is chosen the signal can extend to higher masses.

When applied to signal the algorithm correctly selects the correct $h \rightarrow bb$ pairing between 20-40% of cases depending upon the model. The requirements on these quantities are listed also in Table 1.

Table 1: Signal region definitions for the inclusive A-type SR, alongside the three varying m_{eff} selection regions. The letter appended to the SRA label corresponds to the low, medium or high m_{eff} selection.

Variable	SRA	SRA-L	SRA-M	SRA-H
N_{leptons} (baseline)		$= 0$		
N_{jets}		≥ 6		
$N_{\text{b-jets}}$		≥ 4		
$E_{\text{T}}^{\text{miss}}$ [GeV]		> 250		
min $\Delta\phi(\text{jet}_{1-4}, \mathbf{p}_{\text{T}}^{\text{miss}})$ [rad]		> 0.4		
τ veto		Yes		
$p_{\text{T}}(b_1)$ [GeV]		> 200		
$\Delta R_{\text{max}}(b, b)$		> 2.5		
$\Delta R_{\text{max}-\text{min}}(b, b)$		< 2.5		
$m(h_{\text{cand}})$ [GeV]		> 80		
m_{eff} [TeV]	> 1.0	$\in [1.0, 1.2]$	$\in [1.2, 1.5]$	> 1.5

5.2 SRB selections

The SRB region targets small mass-splitting between the $\tilde{b}_1$ and $\tilde{\chi}_1^0$, in the case of $\Delta m(\tilde{\chi}_2^0, \tilde{\chi}_1^0) = 130$ GeV SUSY models. The presence of an initial state radiation (ISR) jet boosting the bottom squarks, and consequently their decay products, is exploited. To efficiently suppress SM background contributions, events are selected with one non-b-tagged ISR jet with $p_{\text{T}} > 300$ GeV and $E_{\text{T}}^{\text{miss}} > 300$ GeV such that $\Delta\phi(j_1, E_{\text{T}}^{\text{miss}}) > 2.8$. A m_{eff} selection of > 1 TeV is also applied. As the b-jets from $\tilde{b}_1$ decays might have too low momenta to pass the b-jet requirements a different algorithm, aiming to reconstruct both Higgs candidates, is employed. Similarly to the *MaxMin* procedure, the algorithm uses a two-step approach wherein the b-jets in the event are iterated over and the ΔR of every pair of b-jets are calculated. Then, two pairs at a time are identified, ΔR_{bb1} and ΔR_{bb2}. The pairings of b-jets which minimises the largest ΔR of the two b-jet pairs, $\min([\Delta R_{bb1}, \Delta R_{bb2}]_{\text{max}})$, are taken as Higgs candidates. The average mass of the two candidates $m(h_{\text{cand1}}, h_{\text{cand2}})_{\text{avg}}$ is calculated and a requirement is placed on the average mass, corresponding to a window around the Higgs mass: [50, 140] GeV. When applied to the compressed signals targeted by this region the algorithm selects the correct $h \rightarrow bb$ pairings in 39-57% of cases depending upon the signal mass hierachy. The SRB requirements are listed in Table 2.

Table 2: Selections for SRB.

Variable	SRB
N_{leptons} (baseline)	= 0
N_{jets}	≥ 5
$N_{\text{b-jets}}$	≥ 4
$E_{\text{T}}^{\text{miss}}$ [GeV]	> 300
$\min \Delta\phi(\text{jet}_{1-4}, \mathbf{p}_{\text{T}}^{\text{miss}})$ [rad]	> 0.4
τ veto	Yes
$m(h_{\text{cand1}}, h_{\text{cand2}})_{\text{avg}}$ [GeV]	∈ [50, 140]
non-b leading jet	Yes
$p_{\text{T}}(j_1)$ [GeV]	> 300
$\lvert\Delta\phi(j_1, E_{\text{T}}^{\text{miss}})\rvert$ [rad]	> 2.8
m_{eff} [TeV]	> 1

5.3 SRC selections

For constant $\tilde{\chi}_1^0$ mass and compressed ($\tilde{b}_1$,$\tilde{\chi}_2^0$) scenarios, ΔR-based algorithms to reconstruct the Higgs candidates are not effective. Either the b-jets from the $\tilde{b}_1$ decays or arising from the Higgs have soft momenta, hence requirements on $N_{\text{b-jets}}$ as well as the reconstruction algorithms are not effective for these kind of events. In SRC events are required to have at least three b-jets whilst the main discriminating quantity is $\mathcal{S}$. Four overlapping regions (SRC25, SRC27, SRC30 and SRC32) are defined with incremental thresholds on $\mathcal{S}$ as reported in Table 3. The $\mathcal{S}$ variable is effective in rejecting the SM background arising from associated production of a Z boson decaying to neutrinos and heavy-flavour jets.

Table 3: Signal region selections for the C-type SRs targeting the low $m(\tilde{b}_1)$ region of the $m_{\tilde{\chi}_1^0}$ = 60 GeV signal grid.

Variable	SRC25	SRC27	SRC30	SRC32
N_{leptons} (baseline)		= 0		
N_{jets}		≥ 4		
$N_{\text{b-jets}}$		≥ 3		
$E_{\text{T}}^{\text{miss}}$ [GeV]		> 250		
$\min \Delta\phi(\text{jet}_{1-4}, \mathbf{p}_{\text{T}}^{\text{miss}})$ [rad]		> 0.4		
$\mathcal{S}$	> 25	> 27	> 30	> 32

6 Background estimation

There are two main SM backgrounds which are expected to contribute to the yields for the SRs introduced in the previous section. For the SRA and SRB regions the main background is $t\bar{t}$, which contributes between 70-85% depending upon the region considered, and it is dominated by top-quark pairs produced in association with two b-quarks arising from gluon splitting. For the SRC regions the two main backgrounds are $t\bar{t}$ and Z+jets. For the lowest $\mathcal{S}$ selection the $t\bar{t}$ contribution is dominant (33%) with the Z+jets

background subdominant (28%). In the SRs with tighter $\mathcal{S}$ selections the Z+jets background becomes dominant (32-38%) and the contribution from $t\bar{t}$ decreases (12-24%) significantly.

The main SM backgrounds in each SR are determined separately with a profile likelihood fit [77], commonly referred to as a background-only fit. The background-only fit uses the observed event yield in the associated CRs as a constraint to adjust the normalization of the background processes assuming that no signal is present. The normalization factor is referred to as the μ factor. CRs are designed to be enriched in specific background contributions relevant to the analysis, whilst minimising the potential signal contamination, and they are orthogonal to the SRs. The inputs to the background-only fit for each SR include the number of events observed in its associated CR and the number of events predicted by simulation in each region for all background processes. They are both described by Poisson statistics. The systematic uncertainties, described in Section 7, are included in the fit as nuisance parameters. They are constrained by Gaussian distributions with widths corresponding to the sizes of the uncertainties and are treated as correlated, when appropriate, between the various regions. The product of the various probability density functions and the Gaussian distributions forms the likelihood function, which the fit maximizes by adjusting the background normalization and the nuisance parameters. This approach reduces systematic uncertainties as only systematics on the extrapolation from the CRs to the SRs are necessary. Finally, the reliability of the MC extrapolation of the SM background estimates outside of the control regions is evaluated in dedicated validation regions (VR) orthogonal to CRs and SRs.

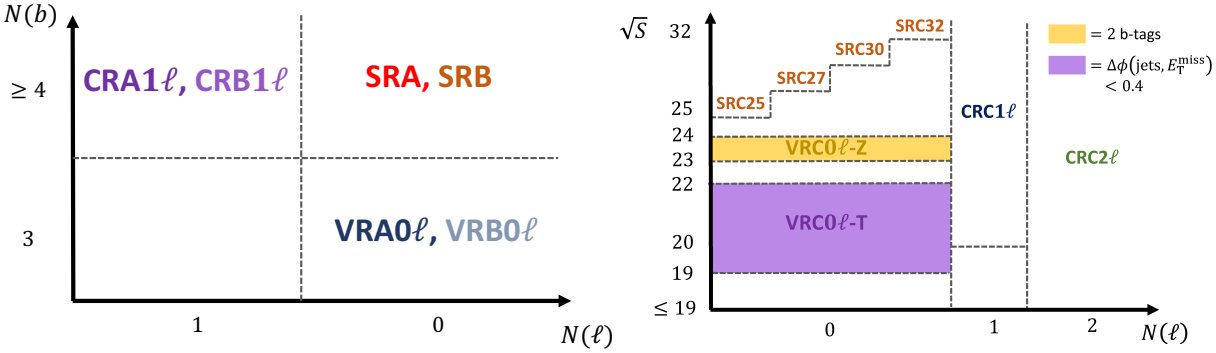

(a) A- and B-type fit strategy

(b) C-type fit strategy

Figure 3: Schematic diagrams of the fit strategies for (left) the A-, B- and (right) C-type regions. Generally the CRs require a different lepton multiplicity than the SRs. The validation regions are defined with a lower b-jet multiplicity requirement, except in the case of the VRC0ℓ-T region, which instead inverts the SR min $\Delta\phi(\text{jet}_{1-4}, \mathbf{p}_{\text{T}}^{\text{miss}})$ selection.

The fit strategies for the A- and B-type regions are very similar and are schematically represented in Figure 3(a), which rely on CRs with a single lepton requirement, as the $t\bar{t}$ background in the SR is dominated by semi-leptonic $t\bar{t}$ decays where the lepton is not identified. The main background in both regions is $t\bar{t}$ pair production in association with heavy flavour jets, which contributes between 68% and 80% in the SRA regions and 88% in the SRB region. The fit strategy for the C-type regions is presented in Figure 3(b). The strategy is different as the the main background in these regions is Z+jets (33% to 38% depending on SR), closely followed by $t\bar{t}$ (20% to 30% depending on SR). In order to define CRs enhanced in $t\bar{t}$ and Z+jets additional variables are used:

- m_{T} [GeV] : the event transverse mass m_{T} is defined as $m_{\text{T}} = \sqrt{2p_{\text{T}}(\ell)E_{\text{T}}^{\text{miss}}(1-\cos(\Delta\phi))}$, where $\Delta\phi$ is the difference in azimuthal angle between the lepton and the $\mathbf{p}_{\text{T}}^{\text{miss}}$, and is used in the one-lepton CRs to reject multi-jet events which can be mis-identified as containing a prompt lepton.

- Contransverse mass (m_{CT}) [GeV] [78]: this variable is used to produce a region that is very pure in the $t\bar{t}$ process. For identical decays of both top-quarks into two visible particles v_1 and v_2 (the b-quarks), and two invisible particles X_1 and X_2 (taken to be the W-bosons decaying to lepton and lepton neutrino), m_{CT} is defined as

$$m_{\mathrm{CT}}^2(v_1,\ v_2) = [E_{\mathrm{T}}(v_1) + E_{\mathrm{T}}(v_2)]^2 - [\mathbf{p}_{\mathrm{T}}(v_1) - \mathbf{p}_{\mathrm{T}}(v_2)]^2.$$

  For $t\bar{t}$ the m_{CT} has an end-point of ≈ 140 GeV; as such a selection of $m_{\mathrm{CT}} < 200$ GeV creates a region very pure in $t\bar{t}$.

- $m_{\ell\ell}$ [GeV]: the invariant mass of the two leptons in the event. As the 2L CR is used to constrain the Z+jets background, the $m_{\ell\ell}$ variable is required to be within the Z-mass window: [86, 116] GeV (used exclusively in the two-lepton CR).

- $\tilde{E}_{\mathrm{T}}^{\mathrm{miss}}$ [GeV]: the "lepton corrected" $E_{\mathrm{T}}^{\mathrm{miss}}$. For the 2L CR the transverse momentum vectors of the leptons are subtracted from the $E_{\mathrm{T}}^{\mathrm{miss}}$ calculation in order to mimic the neutrinos from $Z \rightarrow \nu\nu$ decays (used exclusively in the two-lepton CR).

When designing the CRs and VRs the potential signal contamination is checked in each region to ensure that the SUSY process being targeted is small in the regions. The signal contamination in the CRs is found to be negligible, at the level of $< 1\%$ of the total SM expectation, depending upon the signal mass hierarchy. In the VRs the signal contamination is $< 20\%$ of the total SM expectation, depending upon the signal mass scenario considered.

6.1 A-type CR and VR definitions

Separate control regions which are $t\bar{t}$-dominated (CRA1ℓ) are defined for each of the orthogonal A-type regions, whose m_{eff} selections mirror those of the corresponding SRs, and a CR is defined for the inclusive m_{eff} selection. These CRs are defined similarly to the SR selections (as documented in Table 1) however a single signal lepton (either e or μ), with p_{T} >20 GeV is required in the final state. Further to this, the selections used to isolate the Higgs boson in the SRAs, namely the $\Delta R_{\mathrm{max}}(b,b)$, $\Delta R_{\mathrm{max-min}}(b,b)$ and $m(h_{\mathrm{cand}})$ selections, are not applied in order to increase the number of events in the CR. The leading b-jet p_{T} selection is lowered to > 100 GeV to further increase the number of events in the region, and a selection on the transverse mass of $m_{\mathrm{T}} > 20$ GeV is applied to suppress mis-identified leptons. Such selections result in very pure $t\bar{t}$ CRs, with $t\bar{t}$ contributing more than 80% of the total SM contribution in each of the CRs. The fraction of top-quark pairs produced in association with b-quarks is equivalent to the one of the SRs, and accounts for about 70% of the total $t\bar{t}$ contributions. Figure 4(a) presents the distribution of $m(h_{\mathrm{cand}})$ in the CRA1ℓ, and shows that this variable is well modelled.

Zero-lepton validation regions (VRA0ℓ) are defined for each of the m_{eff} thresholds, and are used to validate the modelling of the $t\bar{t}$ when extrapolating from the one-lepton CRs to zero-lepton regions. The selections used for this are again based upon the SR selections but the VRs are orthogonal due to the b-jet multiplicity selection which requires exactly 3 b-jets. Additionally the $\Delta R_{\mathrm{max}}(b,b)$, $\Delta R_{\mathrm{max-min}}(b,b)$ and $m(h_{\mathrm{cand}})$ selections are not applied in this region. A selection of $\mathcal{S}$ <25 is applied to ensure this region is orthogonal to the SRC regions.

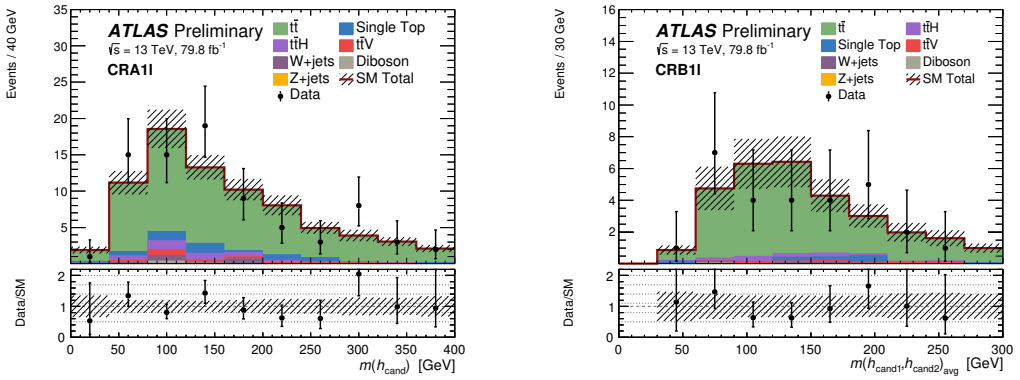

(a) $m(h_{\text{cand}})$ in CRA1ℓ

(b) $m(h_{\text{cand1}}, h_{\text{cand2}})_{\text{avg}}$ in CRB1ℓ

Figure 4: Distributions of (a) the $m(h_{\text{cand}})$ in CRA1ℓ and (b) the $m(h_{\text{cand1}}, h_{\text{cand2}})_{\text{avg}}$ in CRB1ℓ; ratios between SM predictions and data are reported in the bottom panels. All uncertainties as defined in Section 7 are included in the uncertainty bands of top and bottom panels in each plots.

6.2 B-type CR and VR definitions

For the B-type $t\bar{t}$ CR (CRB1ℓ), a similar method of using a one lepton region enriched in $t\bar{t}$ is implemented. The SR selections (as documented in Table 2) are applied, and additionally a single signal lepton with p_{T} > 20 GeV is required. The $m(h_{\text{cand1}}, h_{\text{cand2}})_{avg}$ selection is dropped to increase the number of events in the region, and the $|\Delta\phi(j_1, E_{\text{T}}^{\text{miss}})|$ selection is loosened to > 2.2 to further increase the number of events in the region. Similarly to the A-type CR, a selection of m_{T} > 20 GeV is applied to suppress mis-identified leptons. These selections result in a CR which is very pure with 80% of the total SM expectation consisting of $t\bar{t}$. Figure 4(b) presents the $m(h_{\text{cand1}}, h_{\text{cand2}})_{\text{avg}}$ distribution in this region which is shown to be well modelled.

The associated VR (VRB0ℓ) is defined in a similar manner to the A-type VR, with similar selections to the SRB region, but an exclusive b-jet multiplicity selection of exactly three b-jets. Additionally the selections used to reconstruct the Higgs bosons in the event are dropped to enhance the number of events in the region. A selection of $\mathcal{S}$ <25 is also applied to ensure this region is orthogonal to the C-type SRs.

6.3 C-type CR and VR definitions

Two CRs are defined for the C-type SRs, one to constrain the Z-jets background (CRC2ℓ) and one to constrain the $t\bar{t}$ background (CRC1ℓ). These CRs are based upon the SR shown in Table 3, but are orthogonal due to the different lepton multiplicities required.

The CRC2ℓ requires two same flavour (SF) opposite sign (OS) leptons, with invariant mass in the Z-mass window. The leading lepton is required to have p_{T} >27 GeV while the secondary lepton is required to have p_{T} >20 GeV. The $\tilde{E}_{\text{T}}^{\text{miss}}$ is used, and a selection of $\tilde{E}_{\text{T}}^{\text{miss}}$ > 250 GeV is applied to mimic the $E_{\text{T}}^{\text{miss}}$ selection in the SR. For this region the selections on $\mathcal{S}$ are dropped to enhance the the number of events in the region.

The CRC1ℓ region used to constrain the $t\bar{t}$ background requires one signal lepton with p_{T} >20 GeV. As this region is used to constrain the $t\bar{t}$ background in all of the C-type SRs, a lower limit on $\mathcal{S}$ of > 20 is applied. Similarly as with the A- and B-type CR, a selection of m_{T} >20 GeV is applied to remove the multi-jet contribution with fake or non-prompt leptons.

Two zero-lepton VRs are defined to validate the extrapolation from CR to SR based upon the SR selections. A zero-lepton, two b-jet VR (VRC0ℓ-Z) with $\mathcal{S} \in [23, 24]$ and $m_{\mathrm{CT}} > 200$ GeV ensures a region orthogonal to the SR, but with a large contribution from the Z-jets process. The second VR is used to validate the $t\bar{t}$ modelling (VRC0ℓ-T), with zero-leptons, $\mathcal{S} \in [19, 22]$ and an inverted selection on the min $\Delta\phi(\mathrm{jet}_{1-4}, \mathbf{p}_{\mathrm{T}}^{\mathrm{miss}})$ to ensure orthogonality.

6.4 Summary of CR and VR results

The control region yields and fitted normalization factors μ for the A-, B- and C-type regions are presented in Figure 5. All μ values are consistent with unity, suggesting good modelling of the key SM background processes already at the level of MC predictions. Figure 6 presents the observed yields, background estimates and significance [79] for the A-, B- and C-type validation regions. The background-only fit estimates are in good agreement with the data in these regions, with the post-fit expectation within 1σ of the central value for all regions.

7 Systematic Uncertainties

Several sources of experimental and theoretical systematic uncertainty in the signal and background estimates are considered in this analysis. Their impact is reduced through fitting the event yields and normalising the dominant backgrounds in the control regions defined with kinematic selections resembling those of the corresponding signal region (see Section 6). Uncertainties due to the numbers of events in the CRs are also introduced in the fit for each region. The dominant contributions are summarized in Table 4.

Dominant detector-related systematic uncertainties arise from the b-tagging efficiency and mis-tagging rates, jet energy scale and jet energy resolution. In the SRA regions and the SRB region the contributions of these uncertainties are almost equivalent. In the SRC region the b-tagging uncertainty is dominant. The systematic uncertainty on the b-tagging efficiency ranges from 4.5% for b-jets with $p_{\mathrm{T}} \in [35, 40]$ GeV up to 7.5% for b-jets with larger p_{T}. It is estimated by varying the η-, p_{T}- and flavour-dependent scale factors applied to each jet in the simulation within a range that reflects the systematic uncertainty in the measured tagging efficiency and mis-tag rates in data [66]. The uncertainties in the jet energy scale and resolution are based on their respective measurements in data [63, 80]. The uncertainties associated with lepton reconstruction and energy measurements have a negligible impact on the final results. Lepton, photon and jet-related uncertainties are propagated to the calculation of the $E_{\mathrm{T}}^{\mathrm{miss}}$, and additional uncertainties are included in the energy scale and resolution of the soft term. The systematic uncertainties related to the modelling of the energy of jets and leptons in the simulation are propagated to $\mathcal{S}$. No additional uncertainty related to the modelling of the resolution of these energies, used to evaluate $\mathcal{S}$ as per Equation 2, is applied. This is because the resolutions are taken from simulation when calculating $\mathcal{S}$ both in data and MC, hence uncertainties on their modelling does not effect $\mathcal{S}$.

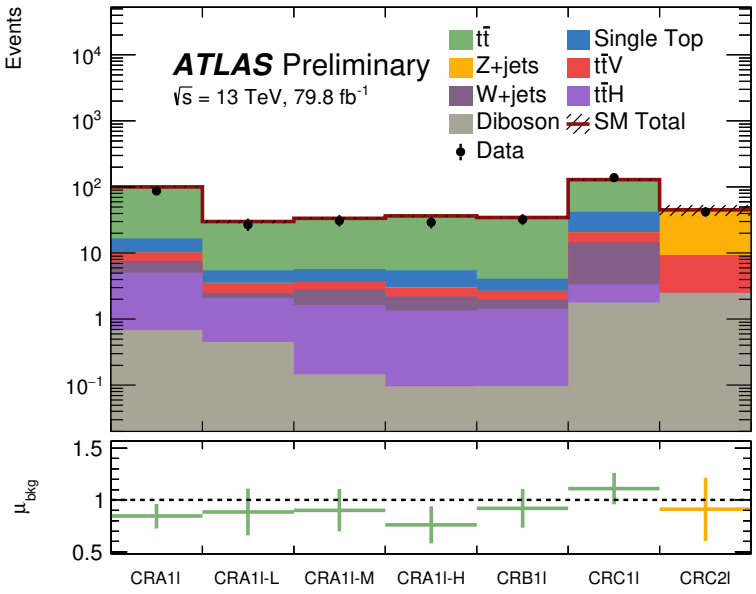

Figure 5: Control region event yields compared to SM MC predictions (top panel) and μ scale factors (bottom panel) for the A-, B- and C-type regions. The uncertainty on the μ factors and the total expected yield include statistical and systematic uncertainties as introduced in Section 7.

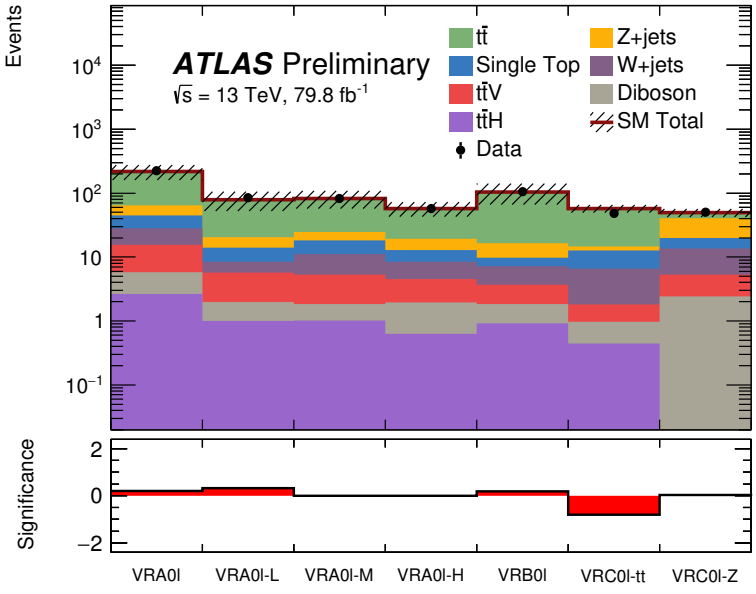

Figure 6: Results of the background-only fit extrapolated to VRs for the A-, B- and C-type regions. The normalization of the backgrounds is obtained from the fit to the CRs. The upper panel shows the observed number of events and the predicted background yields. Statistical and systematic uncertainties as introduced in Section 7 are included in the uncertainty band. The lower panel shows the significance in each VR. The significance calculation is performed as described in Ref. [79].

Uncertainties in the modelling of the SM background processes from MC simulation and their theoretical cross-section uncertainties are also taken into account. The dominant uncertainties in SRAs and SRB arise from theoretical and modelling uncertainties of the top quark pair. They are computed as the difference between the prediction from nominal samples and those from additional samples differing in generator or parameter settings, or using internal weights assigned to the events depending on the choice of scale and PDF. The impact of the PS and hadronisation model is evaluated by comparing the nominal generator with a POWHEG sample interfaced to HERWIG 7 [81, 82], using the H7UE set of tuned parameters [82]. To assess the uncertainty due to the choice of the matching scheme, an aMC@NLO+PYTHIA8 setup is employed, which uses a reoptimised functional form of the shower starting scale $\mu_{\mathrm{q}} = H_{\mathrm{T}}/2$, where H_{T} is defined here as the scalar sum of the p_{T} of all outgoing partons. Finally, to account for the uncertainty on additional b-quark emissions characterising the inclusive NLO setup as used in POWHEG, a 30% uncertainty is assigned to the event for each b-quark not originating from the top [83].

The dominant uncertainties in SRC arise from Z+jets MC modelling followed by uncertainties on $t\bar{t}$ and single-top. The Z+jets (as well as W+jets) modelling uncertainties are estimated by considering different merging (CKKW-L) and resummation scales using alternative samples, PDF variations from the NNPDF30NNLO replicas [42], as well as an envelope formed from seven-point scale variations of the renormalization and factorization scales. The various components are added in quadrature. A 40% uncertainty [84] is assigned to the heavy-flavour jet content in W+jets, estimated from MC simulation in the one-lepton channel control regions. Uncertainties on the single-top-quark (Wt) backgrounds are estimated with an approach equivalent to the one used for $t\bar{t}$. One additional uncertainty stems from the modelling of the interference between the $t\bar{t}$ and Wt processes at NLO [85].

Uncertainties in backgrounds such as diboson and ttV are also estimated by comparisons of the nominal sample with alternative samples differing in generator or parameter settings and contribute less than 5% to the total uncertainty.

For the SUSY signal processes, both the experimental and theoretical uncertainties in the expected signal yield are considered. Experimental uncertainties are found to be between 6% and 36% across the mass plane with fixed LSP mass for A-type SRs and between 4% and 40% for C-type SRs. For models where $\Delta m(\tilde{\chi}_2^0, \tilde{\chi}_1^0) = 130$ GeV is assumed, scenarios where SRB is relevant have uncertainties between 11% and 37%. In all SRs, they are largely dominated by the uncertainty in the b-tagging efficiency. Theoretical uncertainties in the NLO+NLL cross-section are calculated for each SUSY signal scenario and are dominated by the uncertainties in the renormalization and factorization scales, followed by the uncertainty in the PDF. They vary between 15% and 30% for bottom squark masses in the range between 400 GeV and 1300 GeV. Additional uncertainties in the acceptance and efficiency due to the modelling of initial-state radiation and scale variations in SUSY signal MC samples are also taken into account and contribute up to about 10%.

8 Results and Interpretation

The event yields for all signal regions are reported in Table 5. The SM background expectations resulting from background-only fits are also reported showing statistical plus systematic uncertainties. The largest background contribution in A-type and B-type SRs arises from $t\bar{t}$ production, whilst $Z \to \nu\bar{\nu}$ production in association with b-quarks is equivalent to the $t\bar{t}$ contribution for C-type SRs. Other background sources are $t\bar{t}+W/Z$, single-top and W+jets production. The results are also summarized in Figure 7, where

Table 4: Dominant systematic uncertainties on background estimates in A-type and B-type (top table) and C-type (bottom table) regions. Individual uncertainties can be correlated, and do not necessarily add up quadratically to the total background uncertainty. The percentages show the size of the uncertainty relative to the total expected background.

Uncertainty of region	SRA	SRA-L	SRA-M	SRA-H	SRB
Total background expectation	22.8	5.8	9.5	7.5	4.0
Total background error	3.2 (14%)	1.5 (26%)	2.0 (21%)	1.4 (19%)	1.1 (28%)
Systematic, experimental	1.7 (8%)	0.7 (12%)	1.0 (11%)	0.6 (8%)	0.3 (8%)
Systematic, theoretical	2.5 (11%)	1.3 (22%)	1.7 (18%)	1.2 (16%)	0.8 (20%)
Statistical, MC samples	1.2 (5%)	0.6 (10%)	0.8 (8%)	0.7 (9%)	0.5 (13%)

Uncertainty of region	SRC25	SRC27	SRC30	SRC32
Total background expectation	39.8	19.1	8.1	3.3
Total background error	3.9 (10%)	2.3 (12%)	1.5 (19%)	0.7 (21%)
Systematic, experimental	2.8 (7%)	1.4 (7%)	1.1 (14%)	0.5 (16%)
Systematic, theoretical	4.8 (12%)	2.3 (12%)	1.1 (13%)	0.4 (13%)
Statistical, MC samples	<1%	1.2 (6%)	0.9 (11%)	0.4 (12%)

the significance for each of the SRs are also presented. No significant deviations are observed between expected and observed yields in all regions considered.

Figure 8 shows the comparison between the observed data and the SM predictions for some relevant kinematic distributions for the inclusive SRA, SRB and SR C-type selections before specific requirements are applied on the quantity shown. For illustrative purposes, the distributions expected for scenarios with different bottom squark, $\tilde{\chi}_2^0$ and $\tilde{\chi}_1^0$ masses depending on the SR considered are shown.

The CLs technique [86] is used to place 95% Confidence Level (CL) upper limits on contributions from physics beyond the SM (BSM) for each signal region. The profile-likelihood-ratio test statistic is used to exclude the signal-plus-background hypothesis for specific signal models. When normalized by the integrated luminosity of the data sample, results can be interpreted as corresponding upper limits on the visible cross-section, σ_{vis}, defined as the product of the BSM production cross-section, the acceptance and the selection efficiency of a BSM signal. When calculating the model-independent upper limits of the A-type regions only the inclusive SRA region is used. Table 6 summarizes the observed (S_{obs}^{95}) and expected (S_{exp}^{95}) 95% CL upper limits on the number of BSM events and on σ_{vis} for all channels and signal regions. The p_0-values, which represent the probability of the SM background alone to fluctuate to the observed number of events or higher, are also provided and are capped at $p_0 = 0.5$; the associated significance is provided in parentheses.

Exclusion limits are obtained assuming the two types of SUSY particle mass hierarchies described in Section 1. The lightest bottom squark decays exclusively via $\tilde{b}_1 \rightarrow b\tilde{\chi}_2^0$ with subsequent decay $\tilde{\chi}_2^0 \rightarrow h\tilde{\chi}_1^0$. The expected limits from the SRs are compared for each set of scenarios and the observed limits are obtained by choosing the SR with the best expected sensitivity for each SUSY model. Prior to this, a statistical combination of the exclusive A-type SRs is used when deriving the model-dependent limits as this provides greater exclusion in the bottom-squark scenarios considered. The fit procedure takes into account correlations in the yield predictions between control and signal regions due to common background

Table 5: Background-only fit results for the A- and B-type regions (top table) and C-type regions (bottom table) performed using 79.8 fb^{-1}. The post-fit uncertainty shows the total statistical + systematic uncertainty.

	SRA	SRA-L	SRA-M	SRA-H	SRB
Observed events	27	7	12	8	4
Fitted SM bkg events	22.8 ± 3.2	5.8 ± 1.5	9.5 ± 2.0	7.5 ± 1.4	4.0 ± 1.1
$t\bar{t}$	15.3 ± 2.7	4.5 ± 1.4	6.3 ± 1.7	4.7 ± 1.3	3.5 ± 1.2
Z+jets	1.5 ± 0.9	0.3 ± 0.2	0.5 ± 0.2	0.7 ± 0.4	0.09 ± 0.08
Single-top	3.1 ± 0.8	0.4 ± 0.3	1.4 ± 0.5	1.3 ± 0.3	$0.24^{+0.26}_{-0.24}$
$t\bar{t}$ +W/Z	1.1 ± 0.2	0.2 ± 0.1	0.5 ± 0.2	0.4 ± 0.2	0.09 ± 0.07
$t\bar{t}$ +h	1.3 ± 0.2	0.4 ± 0.1	0.5 ± 0.1	0.3 ± 0.1	0.11 ± 0.03
W+jets	0.4 ± 0.3	–	$0.28^{+0.33}_{-0.28}$	0.09 ± 0.02	–
Diboson	0.10 ± 0.05	$0.00^{+0.02}_{-0.00}$	0.10 ± 0.04	–	–

	SRC25	SRC27	SRC30	SRC32
Observed events	43	24	6	1
Fitted SM bkg events	39.8 ± 3.9	19.1 ± 2.3	8.1 ± 1.5	3.3 ± 0.7
$t\bar{t}$	13.1 ± 2.6	4.7 ± 0.9	1.2 ± 0.3	0.4 ± 0.1
Z+jets	11.3 ± 3.0	6.3 ± 1.8	3.1 ± 0.9	1.2 ± 0.4
Single-top	4.3 ± 0.5	2.2 ± 0.2	1.1 ± 0.3	0.3 ± 0.1
$t\bar{t}$ +W/Z	5.0 ± 1.6	2.9 ± 0.9	1.0 ± 0.4	0.5 ± 0.2
$t\bar{t}$ +h	0.33 ± 0.05	0.18 ± 0.03	$0.01^{+0.02}_{-0.01}$	$0.01^{+0.01}_{-0.01}$
W+jets	4.1 ± 0.4	1.7 ± 0.3	1.0 ± 0.3	0.5 ± 0.1
Diboson	1.6 ± 0.4	1.2 ± 0.2	0.6 ± 0.2	0.4 ± 0.3

normalization parameters and systematic uncertainties. The experimental systematic uncertainties in the signal are taken into account for the calculation and are assumed to be fully correlated with those in the SM background.

Figures 9(a) and 9(b) show the observed (solid line) and expected (dashed line) exclusion contours at 95% CL in the $\tilde{b}_1$–$\tilde{\chi}^0_2$ mass planes for the two types of SUSY scenarios considered. For the scenarios where the mass of the neutralino is assumed to be 60 GeV, the sensitivity to models with the largest mass difference between the $\tilde{b}_1$ and the $\tilde{\chi}^0_2$ is achieved with the combination of the A-type SRs. Sensitivity to scenarios with small mass differences is obtained with the dedicated SRCs. For scenarios with $\Delta m(\tilde{\chi}^0_2, \tilde{\chi}^0_1) = 130$ GeV, the sensitivity of the A-type SRs is complemented by the B-type SR in the case of small mass difference between $\tilde{b}_1$ and the $\tilde{\chi}^0_2$. Bottom squark masses up to 1.4 TeV are excluded for models with fixed $m_{\tilde{\chi}^0_1} = 60$ GeV and $\tilde{\chi}^0_2$ masses between 200 and 1200 GeV. It is noted that $\tilde{\chi}^0_2$ masses around 190 GeV are also excluded for $\tilde{b}_1$ masses up to 1 TeV as depicted in Figure 9(b). In case of $\Delta m(\tilde{\chi}^0_2, \tilde{\chi}^0_1) = 130$ GeV, bottom squark masses up to 1.15 TeV are excluded for $\tilde{\chi}^0_2$ masses up 700 GeV. The loss in sensitivity for models where $\tilde{\chi}^0_2$ masses are below 190 GeV is due to the stringent requirements on $E_{\mathrm{T}}^{\mathrm{miss}}$.

The results constitute a large improvement upon previous Run-1 searches and significantly strengthen the constraints on bottom squark masses, being also complementary to other searches where bottom squarks

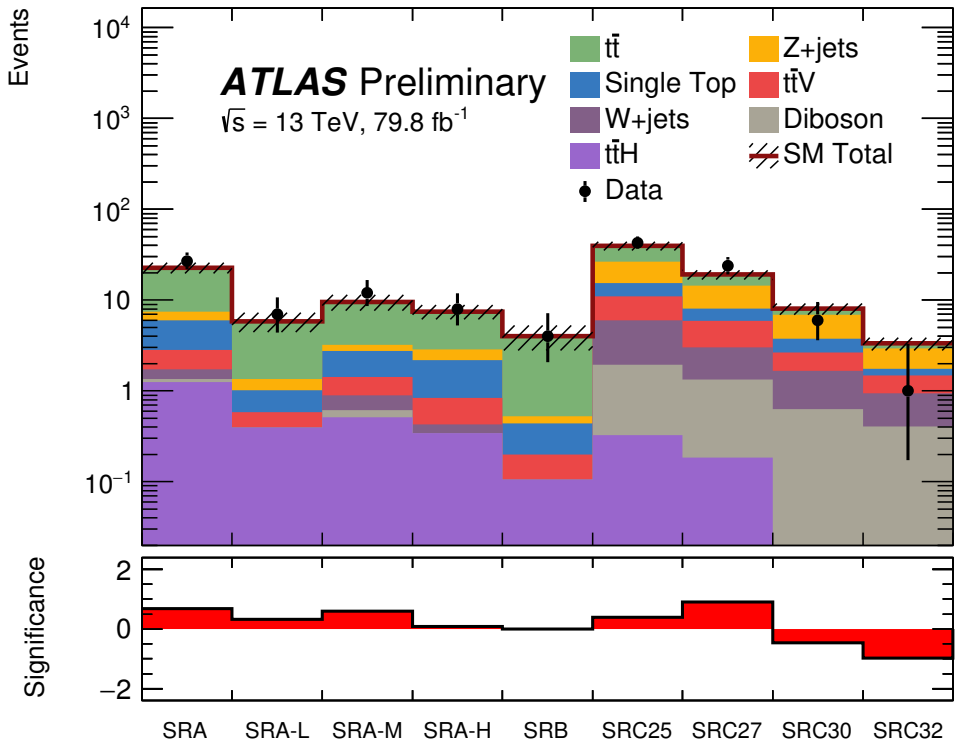

Figure 7: Results of the background-only fit extrapolated to all SRs. The normalization of the backgrounds is obtained from the fit to the CRs. The upper panel shows the observed number of events and the predicted background yields. All uncertainties defined in Section 7 are included in the uncertainty band. The lower panel shows the significance in each SR. The significance calculation is performed as described in Ref. [79].

are assumed to decay directly to $\tilde{\chi}_1^0$ and one b-quark or to top quarks and charginos [87].

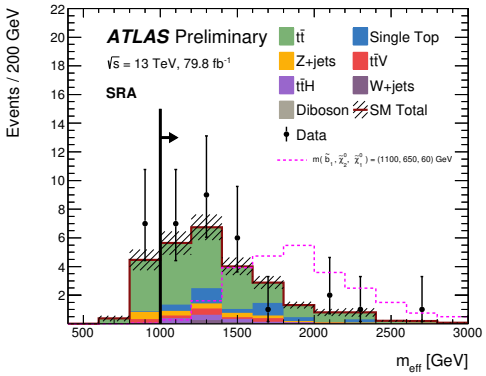

(a) SRA m_{eff}

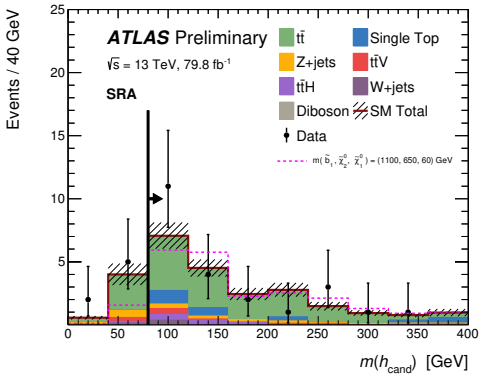

(b) SRA $m(h_{\text{cand}})$

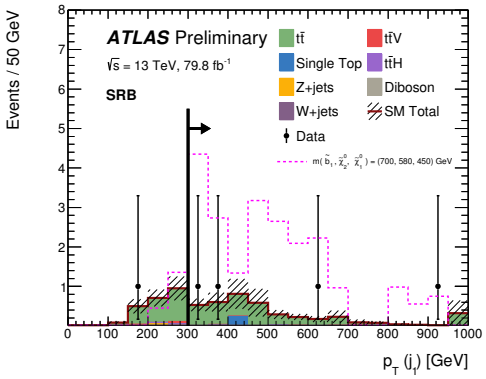

(c) SRB p_{T} (j_1)

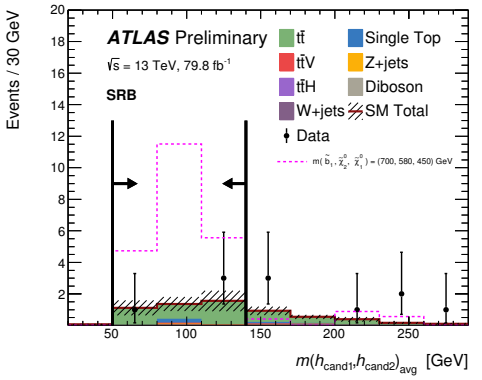

(d) SRB $m(h_{\text{cand1}}, h_{\text{cand2}})_{avg}$

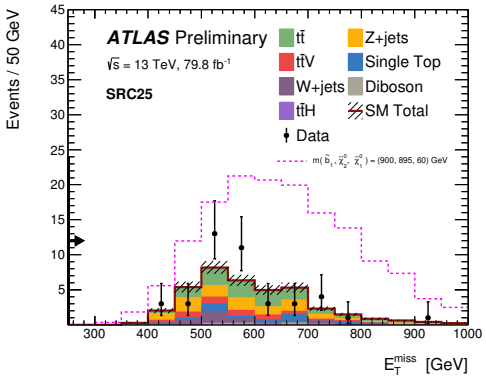

(e) SRC $E_{\text{T}}^{\text{miss}}$

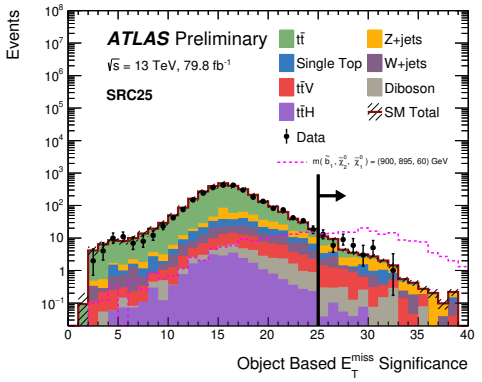

(f) SRC $\mathcal{S}$

Figure 8: Distributions of (a) the m_{eff} and (b) the $m(h_{\text{cand}})$ in the inclusive SRA region; (c) the leading jet p_{T} and (d) the $m(h_{\text{cand1}}, h_{\text{cand2}})_{avg}$ for the average mass of the Higgs candidates in the SRB region; (e) $E_{\text{T}}^{\text{miss}}$ and (f) $\mathcal{S}$ for SR C-type regions. All SR selections are applied except for the selection on the variable shown, where the selection on the variable under consideration is denoted by an arrow, except in the case of (e), where the full SRC selection is applied. All uncertainties as defined in Section 7 are included in the uncertainty band. For illustration, contributions expected for scenarios with different bottom squark, $\tilde{\chi}_2^0$ and $\tilde{\chi}_1^0$ masses depending on the SR considered are superimposed.

Table 6: From left to right, observed 95% CL upper limits, on the visible cross sections σ_{vis}, the observed (S^{95}_{obs}) and expected (S^{95}_{exp}) 95% CL upper limits on the number of signal events with ± 1 σ excursions of the expectaction, the discovery p-value (p_0), truncated at 0.5 and the associated significance (in parentheses).

	σ_{vis}	S^{95}_{obs}	S^{95}_{exp}	p_0-value
SRA (incl)	0.21	16.5	$13.1^{+5.0}_{-2.8}$	0.24 (0.69)
SRA-L	0.09	7.5	$6.7^{+3.5}_{-2.0}$	0.41 (0.24)
SRA-M	0.14	11.0	$8.4^{+3.7}_{-1.6}$	0.25 (0.69)
SRA-H	0.10	7.7	$7.3^{+3.3}_{-2.2}$	0.45 (0.12)
SRB	0.08	6.4	$6.5^{+2.7}_{-2.6}$	0.50 (0.00)
SRC25	0.23	18.7	$15.8^{+6.1}_{-4.0}$	0.28 (0.57)
SRC27	0.20	15.8	$11.7^{+4.7}_{-2.9}$	0.16 (1.01)
SRC30	0.07	5.9	$7.3^{+3.5}_{-2.4}$	0.50 (0.00)
SRC32	0.04	3.2	$5.0^{+2.7}_{-1.6}$	0.50 (0.00)

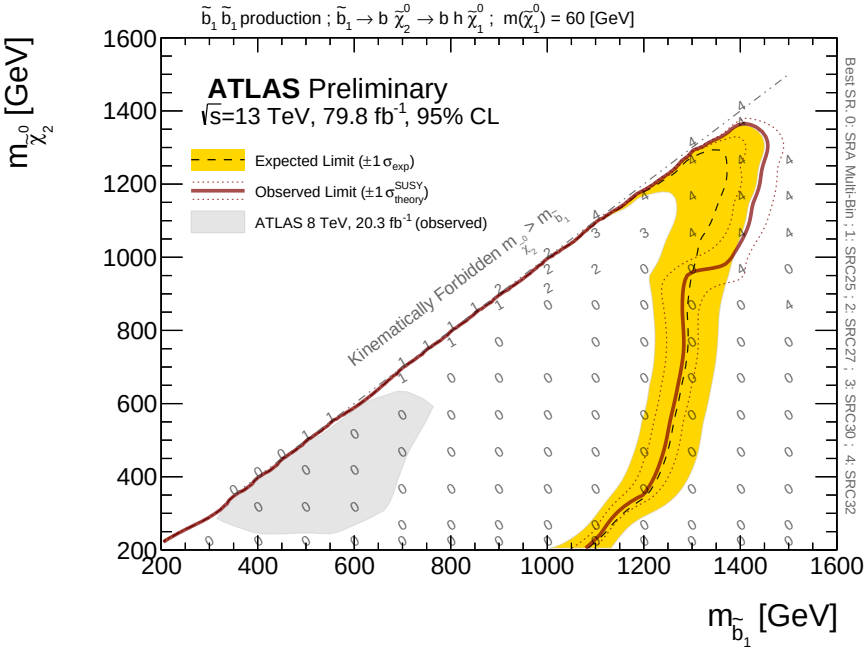

(a) $m(\tilde{\chi}_1^0) = 60\,\text{GeV}$ signal scenario.

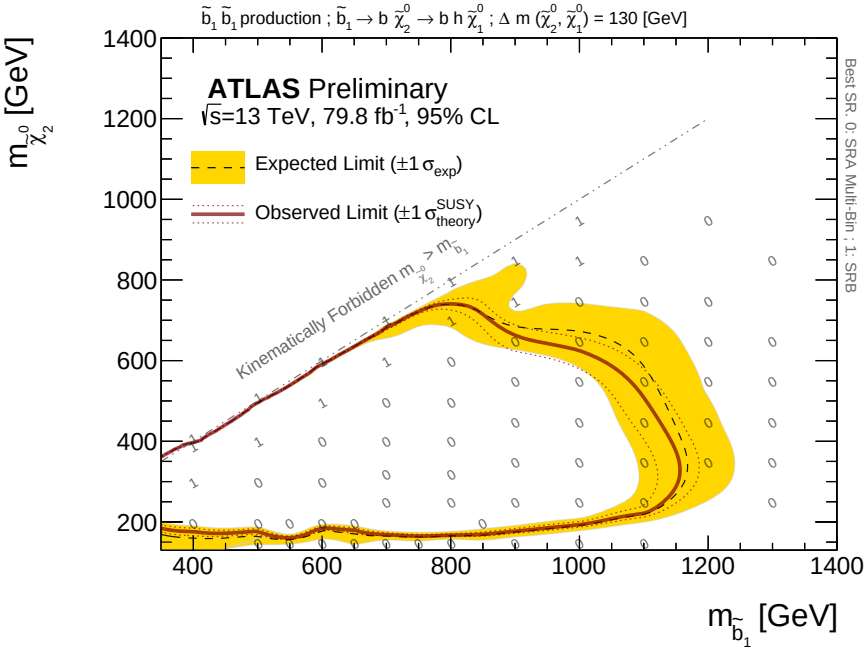

(b) $\Delta m(\tilde{\chi}_2^0, \tilde{\chi}_1^0) = 130\,\text{GeV}$ signal scenario.

Figure 9: Exclusion contour at the 95% CL in the $m(\tilde{b}_1, \tilde{\chi}_2^0)$ phase space for (a) the $m(\tilde{\chi}_1^0) = 60\,\text{GeV}$ signal scenario, ATLAS Run 1 limit taken from Ref. [21] and (b) the $\Delta m(\tilde{\chi}_2^0, \tilde{\chi}_1^0) = 130\,\text{GeV}$ signal scenario, using the SR with the best-expected sensitivity. The grey numbers denote which SR provides the best expected sensitivity for the signal mass hierarchy considered at that point in the plane.

9 Conclusion

The result of a search for pair production of bottom squarks is reported. The analysis uses 79.8 fb^{-1} of pp collisions at $\sqrt{s}$ = 13 TeV collected by the ATLAS experiment at the LHC between 2015 and 2017. R-parity conserving SUSY scenarios where bottom squarks decay to a b-quark and the second lightest neutralino, $\tilde{b}_1 \rightarrow b + \tilde{\chi}_2^0$, with $\tilde{\chi}_2^0$ subsequently decaying to a SM-like Higgs boson and the lightest neutralino, are considered. The search investigates final states containing large missing transverse momentum and three or more b-tagged jets. No significant excess of events above the expected Standard Model background are found and exclusion limits at the 95% confidence level are placed on both the visible cross-section, and on the mass of the bottom squark under various assumptions on the mass hierarchy of the $\tilde{b}_1$, $\tilde{\chi}_2^0$ and $\tilde{\chi}_1^0$. Bottom squark masses up to 1.4 (1.15) TeV and $\tilde{\chi}_2^0$ masses up to 1200 (700) GeV are excluded in models with fixed $m_{\tilde{\chi}_1^0}$ = 60 GeV ($\Delta m(\tilde{\chi}_2^0, \tilde{\chi}_1^0)$ = 130 GeV). This is the first search for these scenarios carried out by ATLAS in Run 2. The results constitute a large improvement upon previous Run-1 searches and significantly strengthen the constraints on bottom squark production.

Appendix

A Signal Region Cutflows

The cross-section and luminosity scaled event yield of signal events after each selection for the three signal region types are reported in the Tables below. Representative signal models are considered for each region.

Table 7: Cutflow of the cross-section and luminosity scaled MC events for the SRA selections, $\tilde{b}_1$, $\tilde{\chi}_2^0$ and $\tilde{\chi}_1^0$ masses of 500, 380 and 250 GeV, respectively.

	Number of events				Scaled to 79.8fb^{-1}			
Variable	SRA	SRA-L	SRA-M	SRA-H	SRA	SRA-L	SRA-M	SRA-H
Total Generated			40000				39740.4	
Primary vertex			39840				38353.56	
Passed $E_{\mathrm{T}}^{\mathrm{miss}}$ Trigger			19036				18638.34	
$E_{\mathrm{T}}^{\mathrm{miss}} > 250$ [GeV]			2640				2642.25	
$N_{\mathrm{jets}} \geq 6$			1801				1851.76	
$N_{\mathrm{b-jets}} \geq 4$			621				619.10	
N_{leptons} (baseline)=0			498				504.14	
$\min \Delta\phi(\mathrm{jet}_{1-4}, \mathbf{p}_{\mathrm{T}}^{\mathrm{miss}}) > 0.4$ [rad]			216				219.87	
$\Delta R_{\mathrm{max}}(b,b)$>2.5			195				197.45	
$\Delta R_{\mathrm{max-min}}(b,b)$<2.5			162				160.52	
$m(h_{\mathrm{cand}}) > 80$ [GeV]			104				104.21	
$p_{\mathrm{T}}(b_1)$> 200 [GeV]			36				36.59	
τ veto			35				35.58	
$m_{\mathrm{eff}} > 1.0$ [TeV]	32	–	–	–	33.09	–	–	–
$m_{\mathrm{eff}} \in [1.0, 1.2]$ [TeV]	–	7	–	–	–	7.23	–	–
$m_{\mathrm{eff}} \in [1.2, 1.5]$ [TeV]	–	–	11	–	–	–	11.50	–
$m_{\mathrm{eff}} > 1.5$ [TeV]	–	–	–	14	–	–	–	14.36

Table 8: Cutflow of the cross-section and luminosity scaled MC events for the SRB selections, $\tilde{b}_1$, $\tilde{\chi}_2^0$ and $\tilde{\chi}_1^0$ masses of 700, 680 and 550 GeV, respectively.

Variable	Number of Events	Scaled to 79.8fb^{-1}
Total Generated	10000	5190.192
Primary vertex	9967	4974.03
Passed $E_{\mathrm{T}}^{\mathrm{miss}}$ Trigger	3973	2065.10
$N_{\mathrm{jets}} \geq 5$	2989	1573.18
$N_{\mathrm{b-jets}} \geq 4$	230	102.34
N_{leptons} (baseline)= 0	206	54.62
min $\Delta\phi(\mathrm{jet}_{1-4}, \mathbf{p}_{\mathrm{T}}^{\mathrm{miss}})$ >0.4	111	48.06
$m(h_{\mathrm{cand1}}, h_{\mathrm{cand2}})_{\mathrm{avg}} \in [50, 140]$ GeV	94	46.22
$p_{\mathrm{T}}(j_1) > 300$ GeV	17	8.44
$m_{\mathrm{eff}} > 1$ TeV	16	7.78
τ veto	15	7.32
non-b leading jet	15	7.32
$\lvert\Delta\phi(j_1, E_{\mathrm{T}}^{\mathrm{miss}})\rvert$ >2.8	13	6.27
$E_{\mathrm{T}}^{\mathrm{miss}} > 300$ GeV	10	4.88

Table 9: Cutflow of the cross-section and luminosity scaled MC events for the SRC selections, $\tilde{b}_1$, $\tilde{\chi}_2^0$ and $\tilde{\chi}_1^0$ masses of 800, 795 and 60 GeV, respectively.

	Number of Events				Scaled to 79.8fb^{-1}			
Variable	SRC25	SRC27	SRC30	SRC32 |	SRC25	SRC27	SRC30	SRC32
No Selections			10000				2200.09	
Cleaning cuts			9963				2175.89	
Pass $E_{\mathrm{T}}^{\mathrm{miss}}$ Trigger			9426				2059.51	
$E_{\mathrm{T}}^{\mathrm{miss}} > 250$ GeV			7614				1668.54	
$N_{\mathrm{jets}} \geq 4$			5494				1214.10	
$N_{\mathrm{b-jets}} \geq 3$			1788				372.22	
N_{leptons} (baseline)=0			1651				345.16	
min $\Delta\phi(\mathrm{jet}_{1-4}, \mathbf{p}_{\mathrm{T}}^{\mathrm{miss}}) > 0.4$[rads]			1442				301.62	
$\mathcal{S} > 25$	749	–	–	–	155.62	–	–	–
$\mathcal{S} > 27$	–	571	–	–	–	119.25	–	–
$\mathcal{S} > 30$	–	–	296	–	–	–	61.44	–
$\mathcal{S} > 32$	–	–	–	156	–	–	–	32.33

B $\mathcal{S}$ Studies

Figure 10 compares the object-based $E_{\mathrm{T}}^{\mathrm{miss}}$ Sig. ($\mathcal{S}$) [76] with the event-based definition of the $E_{\mathrm{T}}^{\mathrm{miss}}$ Sig. ($E_{\mathrm{T}}^{\mathrm{miss}}/\sqrt{E_{\mathrm{T}}}$, where E_{T} is the scalar sum of all of the physics objects which enter the $E_{\mathrm{T}}^{\mathrm{miss}}$ calculation, including the term to account for the soft energy not associated with any objects) and the $E_{\mathrm{T}}^{\mathrm{miss}}$. The analysis finds the $\mathcal{S}$ provides a much greater sensitivity to the signals under consideration than the event-based $E_{\mathrm{T}}^{\mathrm{miss}}$ Sig. and the $E_{\mathrm{T}}^{\mathrm{miss}}$. Figure 11 shows the significance ratios for the three variables combined onto one plot.

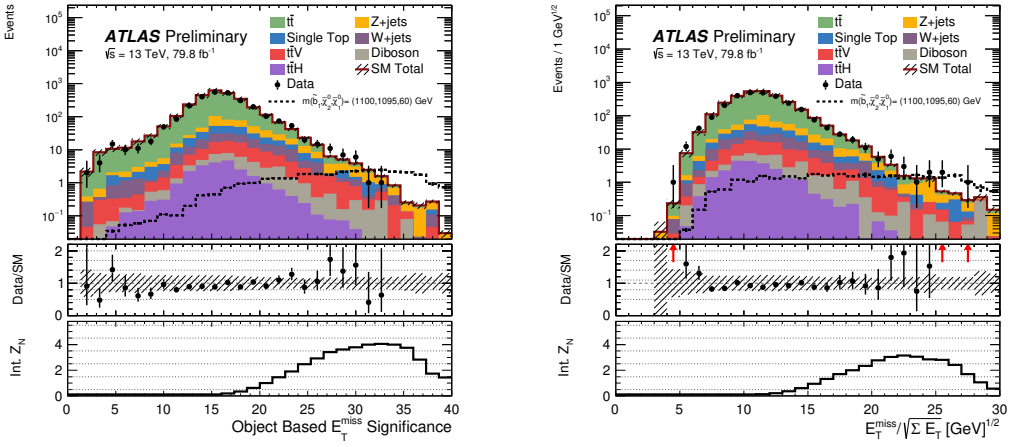

(a) $\mathcal{S}$ (b) $E_{\mathrm{T}}^{\mathrm{miss}}/\sqrt{E_{\mathrm{T}}}$

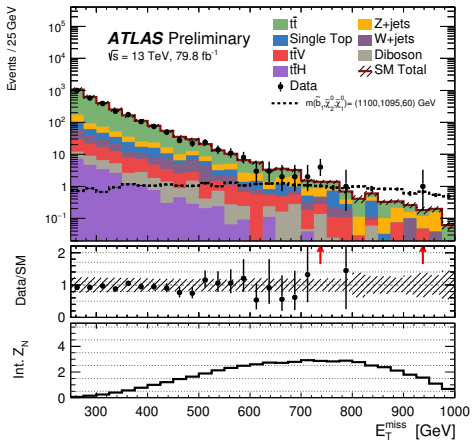

(c) $E_{\mathrm{T}}^{\mathrm{miss}}$

Figure 10: Distributions of (a) $\mathcal{S}$, (b) $E_{\mathrm{T}}^{\mathrm{miss}}/\sqrt{E_{\mathrm{T}}}$ and (c) $E_{\mathrm{T}}^{\mathrm{miss}}$, in the SRC region, without the $\mathcal{S}$ selection applied. All statistical and systematic uncertainties are included. The bottom panel shows the integrated binomial expected significance (Z_N) as a function of the variable, which can be considered as an approximation of the gaussian inversion of the p-value, calculated from the number of SM events predicted, the signal expectation and the error, as described in Ref. [88].

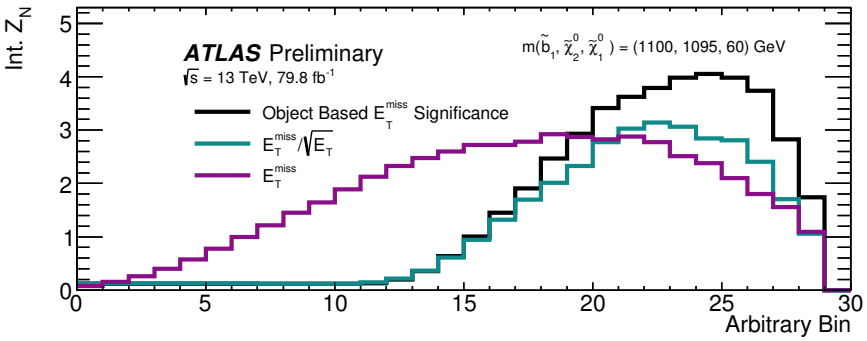

(a)

Figure 11: Integrated binomial expected significance calculated for a scalar bottom signal of $m(\tilde{b}_1, \tilde{\chi}_2^0, \tilde{\chi}_1^0) = (1100, 1095, 60)$ GeV against all standard model backgrounds and using the total uncertainty. The significance as a function of an arbitrary selection for three $E_{\mathrm{T}}^{\mathrm{miss}}$ based variables ($\mathcal{S}$, $E_{\mathrm{T}}^{\mathrm{miss}}/\sqrt{E_{\mathrm{T}}}$ and $E_{\mathrm{T}}^{\mathrm{miss}}$) is shown, in the SRC region, without the $\mathcal{S}$ selection applied.

References

[1] Yu. A. Golfand and E. P. Likhtman, *Extension of the Algebra of Poincare Group Generators and Violation of p Invariance*, JETP Lett. **13** (1971) 323–326, [Pisma Zh. Eksp. Teor. Fiz. **13**, 452 (1971)].

[2] D. V. Volkov and V. P. Akulov, *Is the Neutrino a Goldstone Particle?*, Phys. Lett. B **46** (1973) 109–110.

[3] J. Wess and B. Zumino, *Supergauge Transformations in Four-Dimensions*, Nucl. Phys. B **70** (1974) 39–50.

[4] J. Wess and B. Zumino, *Supergauge Invariant Extension of Quantum Electrodynamics*, Nucl. Phys. B **78** (1974) 1.

[5] S. Ferrara and B. Zumino, *Supergauge Invariant Yang-Mills Theories*, Nucl. Phys. B **79** (1974) 413.

[6] A. Salam and J. A. Strathdee, *Supersymmetry and Nonabelian Gauges*, Phys. Lett. B **51** (1974) 353–355.

[7] N. Sakai, *Naturalness in Supersymmetric Guts*, Z. Phys. C **11** (1981) 153.

[8] S. Dimopoulos, S. Raby, and F. Wilczek, *Supersymmetry and the Scale of Unification*, Phys. Rev. D **24** (1981) 1681–1683.

[9] L. E. Ibanez and G. G. Ross, *Low-Energy Predictions in Supersymmetric Grand Unified Theories*, Phys. Lett. B **105** (1981) 439.

[10] S. Dimopoulos and H. Georgi, *Softly Broken Supersymmetry and SU(5)*, Nucl. Phys. B **193** (1981) 150.

[11] G. R. Farrar and P. Fayet, *Phenomenology of the Production, Decay, and Detection of New Hadronic States Associated with Supersymmetry*, Phys. Lett. B **76** (1978) 575–579.

[12] H. Goldberg, *Constraint on the Photino Mass from Cosmology*, Phys. Rev. Lett. **50** (1983) 1419, [Erratum: Phys. Rev. Lett. **103**, 099905 (2009)].

[13] J. R. Ellis, J. S. Hagelin, D. V. Nanopoulos, K. A. Olive, and M. Srednicki, *Supersymmetric Relics from the Big Bang*, Nucl. Phys. B **238** (1984) 453–476.

[14] R. Barbieri and G. F. Giudice, *Upper Bounds on Supersymmetric Particle Masses*, Nucl. Phys. B **306** (1988) 63.

[15] B. de Carlos and J. A. Casas, *One loop analysis of the electroweak breaking in supersymmetric models and the fine tuning problem*, Phys. Lett. B **309** (1993) 320–328, arXiv:hep-ph/9303291 [hep-ph].

[16] P. Fayet, *Supersymmetry and Weak, Electromagnetic and Strong Interactions*, Phys. Lett. B **64** (1976) 159.

[17] P. Fayet, *Spontaneously Broken Supersymmetric Theories of Weak, Electromagnetic and Strong Interactions*, Phys. Lett. B **69** (1977) 489.

[18] ATLAS Collaboration, *Observation of $H \to b\bar{b}$ decays and VH production with the ATLAS detector*, Jul, 2018. http://cds.cern.ch/record/2630338.

[19] J. Alwall, M.-P. Le, M. Lisanti, and J. G. Wacker, *Searching for Directly Decaying Gluinos at the Tevatron*, Phys. Lett. B **666** (2008) 34–37, arXiv:0803.0019 [hep-ph].

[20] J. Alwall, P. Schuster, and N. Toro, *Simplified Models for a First Characterization of New Physics at the LHC*, Phys. Rev. D **79** (2009) 075020, arXiv:0810.3921 [hep-ph].

[21] ATLAS Collaboration, ATLAS Collaboration, *ATLAS Run 1 searches for direct pair production of third-generation squarks at the Large Hadron Collider*, Eur. Phys. J. C **75** (2015) 510, arXiv:1506.08616 [hep-ex], [Erratum: Eur. Phys. J. C **76**, no.3, 153 (2016)].

[22] CMS Collaboration, CMS Collaboration, *Search for supersymmetry with Higgs boson to diphoton decays using the razor variables at* $\sqrt{s}$ *= 13 TeV*, Phys. Lett. B **779** (2018) 166–190, arXiv:1709.00384 [hep-ex].

[23] ATLAS Collaboration, *The ATLAS Experiment at the CERN Large Hadron Collider*, JINST **3** (2008) S08003.

[24] ATLAS Collaboration, *ATLAS Insertable B-Layer Technical Design Report*, ATLAS-TDR-19, 2010, http://cds.cern.ch/record/1291633, Addendum: ATLAS-TDR-19-ADD-1, 2012, http://cds.cern.ch/record/1451888.

[25] ATLAS Collaboration, *Performance of the ATLAS Trigger System in 2015*, Eur. Phys. J. C **77** (2017) 317, arXiv:1611.09661 [hep-ex].

[26] ATLAS Collaboration, *Luminosity determination in pp collisions at* $\sqrt{s}$ = 8 *TeV using the ATLAS detector at the LHC*, Eur. Phys. J. C **76** (2016) 653, arXiv:1608.03953 [hep-ex].

[27] ATLAS Collaboration, *2015 start-up trigger menu and initial performance assessment of the ATLAS trigger using Run-2 data*, ATL-DAQ-PUB-2016-001, 2016, https://cds.cern.ch/record/2136007.

[28] ATLAS Collaboration, *The ATLAS Simulation Infrastructure*, Eur. Phys. J. C **70** (2010) 823, arXiv:1005.4568 [physics.ins-det].

[29] S. Agostinelli et al. (GEANT4), *GEANT4: A simulation toolkit*, Nucl. Instrum. Meth. A **506** (2003) 250.

[30] ATLAS Collaboration, *The simulation principle and performance of the ATLAS fast calorimeter simulation FastCaloSim*, ATL-PHYS-PUB-2010-013, 2010, https://cds.cern.ch/record/1300517.

[31] J. Alwall et al., *The automated computation of tree-level and next-to-leading order differential cross sections, and their matching to parton shower simulations*, JHEP **07** (2014) 079, arXiv:1405.0301 [hep-ph].

[32] T. Sjöstrand, S. Ask, J. R. Christiansen, R. Corke, N. Desai, P. Ilten, S. Mrenna, S. Prestel, C. O. Rasmussen, and P. Z. Skands, *An Introduction to PYTHIA 8.2*, Comput. Phys. Commun. **191** (2015) 159, arXiv:1410.3012 [hep-ph].

[33] ATLAS Collaboration, *ATLAS Pythia 8 tunes to 7 TeV data*, ATL-PHYS-PUB-2014-021, 2014, https://cds.cern.ch/record/1966419.

[34] L. Lönnblad and S. Prestel, *Merging Multi-leg NLO Matrix Elements with Parton Showers*, JHEP **03** (2013) 166, arXiv:1211.7278 [hep-ph].

[35] R. D. Ball et al., *Parton distributions with LHC data*, Nucl. Phys. B **867** (2013) 244, arXiv:1207.1303 [hep-ph].

[36] W. Beenakker, R. Hopker, M. Spira, and P. Zerwas, *Squark and gluino production at hadron colliders*, Nucl. Phys. B **492** (1997) 51–103, arXiv:hep-ph/9610490 [hep-ph].

[37] W. Beenakker, S. Brensing, M. Kramer, A. Kulesza, E. Laenen, and I. Niessen, *Supersymmetric top and bottom squark production at hadron colliders*, JHEP **08** (2010) 098, arXiv:1006.4771 [hep-ph].

[38] W. Beenakker et al., *Squark and gluino hadroproduction*, Int. J. Mod. Phys. A **26** (2011) 2637–2664, arXiv:1105.1110 [hep-ph].

[39] C. Borschensky, M. Kramer, A. Kulesza, M. Mangano, S. Padhi, T. Plehn, and X. Portell, *Squark and gluino production cross sections in pp collisions at $\sqrt{s}$ = 13, 14, 33 and 100 TeV*, Eur. Phys. J. C **74** (2014) 3174, arXiv:1407.5066 [hep-ph].

[40] S. Alioli, P. Nason, C. Oleari, and E. Re, *A general framework for implementing NLO calculations in shower Monte Carlo programs: the POWHEG BOX*, JHEP **06** (2010) 043, arXiv:1002.2581 [hep-ph].

[41] ATLAS Collaboration, *Further studies on simulation of top-quark production for the ATLAS experiment at $\sqrt{s}$ = 13 TeV*, ATL-PHYS-PUB-2016-016, 2016, https://cds.cern.ch/record/2205262.

[42] T. Gleisberg et al., *Event generation with SHERPA 1.1*, JHEP **02** (2009) 007, arXiv:0811.4622 [hep-ph].

[43] T. Gleisberg and S. Höche, *Comix, a new matrix element generator*, JHEP **12** (2008) 039, arXiv:0808.3674 [hep-ph].

[44] F. Cascioli, P. Maierhofer, and S. Pozzorini, *Scattering Amplitudes with Open Loops*, Phys. Rev. Lett. **108** (2012) 111601, arXiv:1111.5206 [hep-ph].

[45] S. Schumann and F. Krauss, *A Parton shower algorithm based on Catani-Seymour dipole factorisation*, JHEP **03** (2008) 038, arXiv:0709.1027 [hep-ph].

[46] S. Höche, F. Krauss, M. Schönherr, and F. Siegert, *QCD matrix elements + parton showers: The NLO case*, JHEP **04** (2013) 027, arXiv:1207.5030 [hep-ph].

[47] ATLAS Collaboration, ATLAS Collaboration, *Search for squarks and gluinos with the ATLAS detector in final states with jets and missing transverse momentum using 4.7 fb^{-1} of $\sqrt{s}$ = 7 TeV proton-proton collision data*, Phys. Rev. D **87** (2013) 012008, arXiv:1208.0949 [hep-ex].

[48] M. Beneke, P. Falgari, S. Klein, and C. Schwinn, *Hadronic top-quark pair production with NNLL threshold resummation*, Nucl. Phys. B **855** (2012) 695–741, arXiv:1109.1536 [hep-ph].

[49] M. Cacciari, M. Czakon, M. Mangano, A. Mitov, and P. Nason, *Top-pair production at hadron colliders with next-to-next-to-leading logarithmic soft-gluon resummation*, Phys. Lett. B **710** (2012) 612–622, arXiv:1111.5869 [hep-ph].

[50] P. Bärnreuther, M. Czakon, and A. Mitov, *Percent Level Precision Physics at the Tevatron: First Genuine NNLO QCD Corrections to $q\bar{q} \to t\bar{t} + X$*, Phys. Rev. Lett. **109** (2012) 132001, arXiv:1204.5201 [hep-ph].

[51] M. Czakon and A. Mitov, *NNLO corrections to top-pair production at hadron colliders: the all-fermionic scattering channels*, JHEP **12** (2012) 054, arXiv:1207.0236 [hep-ph].

[52] M. Czakon and A. Mitov, *NNLO corrections to top pair production at hadron colliders: the quark-gluon reaction*, JHEP **01** (2013) 080, arXiv:1210.6832 [hep-ph].

[53] M. Czakon, P. Fiedler, and A. Mitov, *Total Top-Quark Pair-Production Cross Section at Hadron Colliders Through $O(\alpha_S^4)$*, Phys. Rev. Lett. **110** (2013) 252004, arXiv:1303.6254 [hep-ph].

[54] M. Czakon and A. Mitov, *Top++: A Program for the Calculation of the Top-Pair Cross-Section at Hadron Colliders*, Comput. Phys. Commun. **185** (2014) 2930, arXiv:1112.5675 [hep-ph].

[55] N. Kidonakis, *Next-to-next-to-leading-order collinear and soft gluon corrections for t-channel single top quark production*, Phys. Rev. D **83** (2011) 091503, arXiv:1103.2792 [hep-ph].

[56] N. Kidonakis, *NNLL resummation for s-channel single top quark production*, Phys. Rev. D **81** (2010) 054028, arXiv:1001.5034 [hep-ph].

[57] N. Kidonakis, *Two-loop soft anomalous dimensions for single top quark associated production with a W- or H-*, Phys. Rev. D **82** (2010) 054018, arXiv:1005.4451 [hep-ph].

[58] D. J. Lange, *The EvtGen particle decay simulation package*, Nucl. Instrum. Meth. A **462** (2001) 152.

[59] ATLAS Collaboration, *Vertex Reconstruction Performance of the ATLAS Detector at $\sqrt{s}$ = 13 TeV*, ATL-PHYS-PUB-2015-026, 2015, https://cds.cern.ch/record/2037717.

[60] ATLAS Collaboration, *Topological cell clustering in the ATLAS calorimeters and its performance in LHC Run 1*, Eur. Phys. J. C **77** (2016) 490, arXiv:1603.02934 [hep-ex].

[61] M. Cacciari, G. P. Salam, and G. Soyez, *The Anti-k(t) jet clustering algorithm*, JHEP **04** (2008) 063, arXiv:0802.1189 [hep-ph].

[62] M. Cacciari, G. P. Salam, and G. Soyez, *FastJet User Manual*, Eur. Phys. J. C **72** (2012) 1896, arXiv:1111.6097 [hep-ph].

[63] ATLAS Collaboration, *Jet energy scale measurements and their systematic uncertainties in proton–proton collisions at $\sqrt{s}$ = 13 TeV with the ATLAS detector*, Phys. Rev. D **96** (2017) 072002, arXiv:1703.09665 [hep-ex].

[64] ATLAS Collaboration, *Selection of jets produced in 13TeV proton-proton collisions with the ATLAS detector*, Jul, 2015. https://cds.cern.ch/record/2037702.

[65] ATLAS Collaboration, *Constituent-level pile-up mitigation techniques in ATLAS*, Aug, 2017. https://cds.cern.ch/record/2281055.

[66] ATLAS Collaboration, *Performance of b-jet identification in the ATLAS experiment*, JINST **11** (2016) P04008, arXiv:1512.01094 [hep-ex].

[67] ATLAS Collaboration, *Electron efficiency measurements with the ATLAS detector using 2012 LHC proton–proton collision data*, Eur. Phys. J. C **77** (2017) 195, arXiv:1612.01456 [hep-ex].

[68] ATLAS Collaboration, *Electron and photon energy calibration with the ATLAS detector using LHC Run 1 data*, Eur. Phys. J. C **74** (2014) 3071, arXiv:1407.5063 [hep-ex].

[69] ATLAS Collaboration, *Electron identification measurements in ATLAS using $\sqrt{s}$ = 13 TeV data with 50 ns bunch spacing*, ATL-PHYS-PUB-2015-041, 2015, https://cds.cern.ch/record/2048202.

[70] ATLAS Collaboration, *Muon reconstruction performance of the ATLAS detector in proton–proton collision data at $\sqrt{s}$ = 13 TeV*, Eur. Phys. J. C **76** (2016) 292, arXiv:1603.05598 [hep-ex].

[71] ATLAS Collaboration, *Measurement of the $t\bar{t}$ production cross-section using $e\mu$ events with b-tagged jets in pp collisions at $\sqrt{s}$ = 13 TeV with the ATLAS detector*, Phys. Lett. B **761** (2016) 136, arXiv:1606.02699 [hep-ex].

[72] ATLAS Collaboration, *Photon identification in 2015 ATLAS data*, Aug, 2016. https://cds.cern.ch/record/2203125.

[73] ATLAS Collaboration, *E_T^{miss} performance in the ATLAS detector using 2015-2016 LHC p-p collisions*, Jun, 2018. http://cds.cern.ch/record/2625233.

[74] ATLAS Collaboration, *Performance of algorithms that reconstruct missing transverse momentum in $\sqrt{s}$ = 8 TeV proton–proton collisions in the ATLAS detector*, Eur. Phys. J. C **77** (2017) 241, arXiv:1609.09324 [hep-ex].

[75] ATLAS Collaboration, *Jet energy measurement with the ATLAS detector in proton–proton collisions at $\sqrt{s}$ = 7 TeV*, Eur. Phys. J. C **73** (2013) 2304, arXiv:1112.6426 [hep-ex].

[76] ATLAS Collaboration, *Object-based missing transverse momentum significance in the ATLAS detector*, Jul, 2018. http://cds.cern.ch/record/2630948.

[77] M. Baak et al., *HistFitter software framework for statistical data analysis*, Eur. Phys. J. C **75** (2015) 153, arXiv:1410.1280 [hep-ex].

[78] D. R. Tovey, *On measuring the masses of pair-produced semi-invisibly decaying particles at hadron colliders*, JHEP **04** (2008) 034, arXiv:0802.2879 [hep-ph].

[79] G. Choudalakis and D. Casadei, *Plotting the differences between data and expectation*, European Physical Journal Plus **127** (2012) 25, arXiv:1111.2062 [physics.data-an].

[80] ATLAS Collaboration, *Jet energy resolution in proton–proton collisions at $\sqrt{s}$ = 7 TeV recorded in 2010 with the ATLAS detector*, Eur. Phys. J. C **73** (2013) 2306, arXiv:1210.6210 [hep-ex].

[81] M. Bähr et al., *Herwig++ Physics and Manual*, Eur. Phys. J. C **58** (2008) 639, arXiv:0803.0883.

[82] J. Bellm et al., *Herwig 7.0/Herwig++ 3.0 release note*, Eur. Phys. J. C **76** (2016) 196, arXiv:1512.01178 [hep-ph].

[83] ATLAS Collaboration, *Improvements in $t\bar{t}$ modelling using NLO+PS Monte Carlo generators for Run2*, Jun, 2018. https://cds.cern.ch/record/2624546.

[84] ATLAS Collaboration, *Measurement of the cross section for the production of a W boson in association with b-jets in pp collisions at $\sqrt{s}$ = 7 TeV with the ATLAS detector*, Phys. Lett. B **707** (2012) 418, arXiv:1109.1470 [hep-ex].

[85] ATLAS Collaboration, *Probing the quantum interference between singly and doubly resonant top-quark production in pp collisions at $\sqrt{s}$ = 13 TeV with the ATLAS detector*, Submitted to: Phys. Rev. Lett. (2018), arXiv:1806.04667 [hep-ex].

[86] A. L. Read, *Presentation of search results: The CL(s) technique*, J. Phys. G **28** (2002) 2693.

[87] ATLAS Collaboration, ATLAS Collaboration, *Search for supersymmetry in events with b-tagged jets and missing transverse momentum in pp collisions at* $\sqrt{s}$ = 13 *TeV with the ATLAS detector*, JHEP **11** (2017) 195, arXiv:1708.09266 [hep-ex].

[88] K. Cranmer, *Practical Statistics for the LHC*, pp. , 267–308. 2015. arXiv:1503.07622 [physics.data-an]. https://inspirehep.net/record/1356277/files/arXiv:1503.07622.pdf. [,247(2015)].